Studying Auroral Microphysics Using Multiple Optically Tracked Rocket Sub-Payloads

By

Joshua M. Vann, B.S.

A Project Submitted in Partial Fulfillment of the Requirements
for the Degree of

Master of Science

in

Physics

University of Alaska Fairbanks

December 2018

APPROVED BY:

Dr. Peter Delamere, Committee Member

Dr. Donald Hampton, Committee Member

Dr. Mark Conde, Committee Chair

Dr. Renate Wackerbauer, Chair

Department of Physics

Abstract

There is insufficient knowledge of scale length parameters associated with ionospheric plasma structures. Using a novel technique combining rocket-based instrument data with ground-based optical and instrumental data measurements, ISINGLASS attempts to determine the spatial scale lengths over which parameter differences in auroral arcs present in the upper ionosphere. Determination of such scale lengths has the propensity to strengthen preexisting models of magnetosphere-ionosphere interactions. While analysis is not complete and the extent of such scale lengths is still unknown, after completion of the experiment phase of the mission, differences in measurements have been found that cannot be accounted for through experimental error. This shows the existence of a critical scale length within the distances measured, and the techniques used present a reliable method with which to launch a future campaign.

.

Acknowledgements

This project would not be possible without the ISINGLASS NASA grant: NNX14AH07G**.** Thank you to my committee and the Physics Department, for countless hours of editing and encouragement, without whom I could not have done this. Thank you to Lucas Hurd and the Toolik Staff for company and troubleshooting help in Toolik, to Caleb Gordon in Coldfoot, Jason Ahrms and Guy Grubbs in Venetie and Donald Hampton in Poker for providing images and countless hours of standing by. Lastly, I want to thank Professor Kristina Lynch for being the Principle Investigator on this project and providing help with updated images and guidance through the final process.

Table of Contents

List of Figures, Tables, Appendices

Chapter 1: Background

1.1 Auroral Background

The aurora is an important part of life in the north, and while the general physical processes that cause these magnificent displays have been understood for some time, many details are still unknown. Specifically, how auroral curtains can be so thin and how they behave is a topic of discussion among scientists. The aurora is the emission of visible light from atoms and molecules in the atmosphere as electrons collide and excite them. The electrons carry energy arising from acceleration in part from the interaction of the solar wind and our magnetosphere. This interaction is complicated, but ultimately transportation occurs through magnetosphere-ionosphere coupling.

Auroral processes can be classified into quasistatic, Alfvénic, and pulsating auroral types (*Paschmann,* 2002; *Newell et al.,* 2009). Within these broad classifications, there exist many subtypes which vary with time, and many interesting events combine multiple types, often either co-located or transitioning from one to another over time (*Mella et al.,* 2011; *Hull et al.,* 2010). Substorms are a common display of Alfvénic aurora, an abrupt increase in nightside hemispheric auroral power (*Akasofu*, 1964). The subtype refers to the acceleration mechanism, not the movement itself. In all cases, electrons are accelerated, however the mechanism is different. For Alfvénic acceleration events, the principal mechanism is electron trapping and subsequent wave-breaking, a process in which instabilities arise and quickly dissipate, moving at the Alfvén speed (*Hui & Seyler,* 1992). Unlike substorms and other alfvénic displays, quasistatic type events are the narrow arcs that move slowly, indicating the acceleration of cold ionospheric electrons from the top of the ionosphere through field-aligned currents. Because there are many different scales of aurora, from 1000's of km down to sub-km scale, the question to be answered will be how the different scales impact dynamics in the magnetosphere.

1.2 Ionospheric Physics: Chemistry and Conduction

The ionosphere is the region of Earth's atmosphere in which a fraction of the atoms/molecules exist in ionic form. In order to understand models of ionospheric-magnetospheric interactions, it is important to outline specific processes occurring in the ionosphere. There are

many more interactions than can be described here, however in an attempt to maintain simplicity, only simple chemistry and relevant energy transport methods will be discussed.

The ionosphere consists of atomic and molecular species that are present in ionic forms. These species interact in many different and complex ways. While the number of species is numerous, a large proportion of those present in the ionosphere are ions of nitrogen, oxygen, and hydrogen (*Banks & Kockarts*, 1973). Some examples are NO, N, N_2, O_2, and H. Energy can flow in the form of electron transfer and kinetic energy, shown through interactions between molecules. There exist many production and loss mechanisms, all of which affect parameters to be investigated in this study such as plasma density and ion flow. Because of this, it is important to be aware of different molecular reactions, with the understanding that they will happen at different rates between the E/F region of the Ionosphere, and have importance to models. Some examples of reactions between these species are those that create NO^+, charge exchange reactions, and recombination reactions (*Torr & Torr*, 1973).

Those that create NO^+:

$$N_2 + O^+ \rightarrow NO^+ + N$$
$$N_2^+ + O \rightarrow NO^+ + N \quad (1)$$

Charge Exchange Reactions:

$$O^+ + H \leftrightharpoons O + H^+$$
$$O^+ + O_2 \rightarrow O_2^+ + O \quad (2)$$

Recombination Reactions:

$$NO^+ + e^- \rightarrow N + O$$
$$O_2 + e^- \rightarrow O + O \quad (3)$$

When looking at molecular interactions in the ionosphere, either neutrals collide, ions collide, or a mixed reaction occurs. The above reactions all represent mixed reactions. When neutrals collide, no charge exchange occurs. Similarly, ionic species interacting rarely transfer charge. The most interesting interaction is seen when a neutral and ion interact. These interactions can be categorized into two different speed types: slow and fast. Slow interactions allow time for an induced dipole, and can often create new species. Fast interactions on the other hand often lead

to charge exchange between the species (*Banks & Kockarts*, 1973). While these interactions themselves are not key to the analysis in this report, they do lead to a basic understanding of the physical processes in the ionosphere, and are useful when discussing the coupling between the magnetosphere and ionosphere present in specific models such as Zettergren to be discussed later in this section.

Another important factor in ionospheric physics is conductivity. Electrical conductivity relates current flow with electric field, and can be thought of as how easily electrons and ions flow within materials. A similar property, thermal conductance, represents the flow of heat within a material. In the ionosphere, three specific types of conductivities are Hall conductivity. Pederson conductivity, and ordinary conductivity. These different conductivities represent directional factors and arise under different conditions such as altitude, pressure, and temperature. The Pederson conductivity conducts current in the direction of the external electric field and perpendicular to the magnetic field. The Hall conductivity conducts current perpendicular to both the electric and magnetic fields. The ordinary conductivity arises when the electric field is applied along the magnetic field, and is therefore unaffected by the magnetic field (*Parks,* 2004). The Figure below shows the altitude in which specific conductivities dominate. For the purpose of this study, the ionosphere is the primary focus, so the ordinary term ($\sigma_{\shortparallel}$) dominates at higher altitudes, the Pederson term (σ_P) dominates at middle altitudes and the Hall term (σ_H) dominates at lower altitude. The differences arise with the plasma in the magnetic field experiencing different types of interactions and collisional cross sections, and the conductivity is anisotropic, meaning that it depends on the direction of the applied electric field. This can be represented by a tensor quantity, and depends still on multiple directions, though the influence is different for each term. The Hall and Pederson currents demonstrate important phenomena present in the auroral current system (*Parks,* 2004) relative to this study.

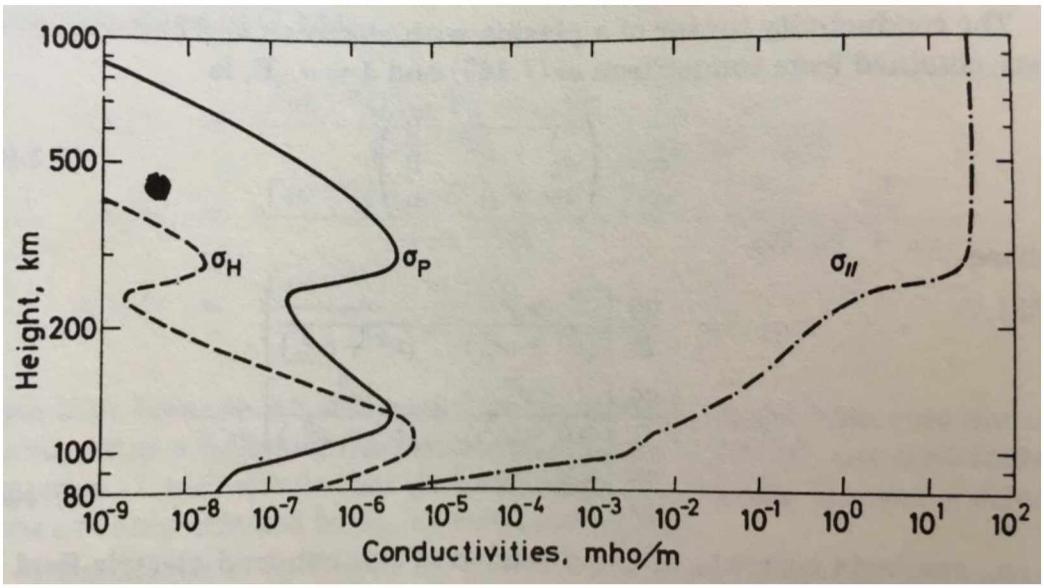

Figure 1: Altitudes where Hall and Pederson conductivities dominate. Image from (*Parks*, 2004).

1.3 Magnetospheric Physics

The magnetosphere is the region above the ionosphere in which electromagnetic fields and space plasma properties are influenced by Earth's magnetic field. Many models of the magnetosphere rely on steady state approximations and relate the flow of plasma by **E** x **B** drift through the magnetosphere (*Wolf*, 1975).

While there are many relationships used by physicists, a simple model of the magnetosphere is shown in Figure 2 below, where the magnetosphere can be seen to be smaller on the sunward side, with an elongated magnetotail on the other side, where reconnection, the meeting point of antiparallel magnetic field lines on an ion-kinetic scale, is prone to occur. The importance to this study is that the aurora is generated by deflection of solar wind, causing charges to flow within the magnetosphere, and interact with the ionosphere, resulting in electron impact excitation. This primary excitation of electrons (1-10 keV) leads to secondary electron excitation (~20eV) through a string of ionizing reactions, causing species in the ionosphere to fluoresce, emitting the light that we see and showing us a picture of the energy interactions happening in the magnetosphere.

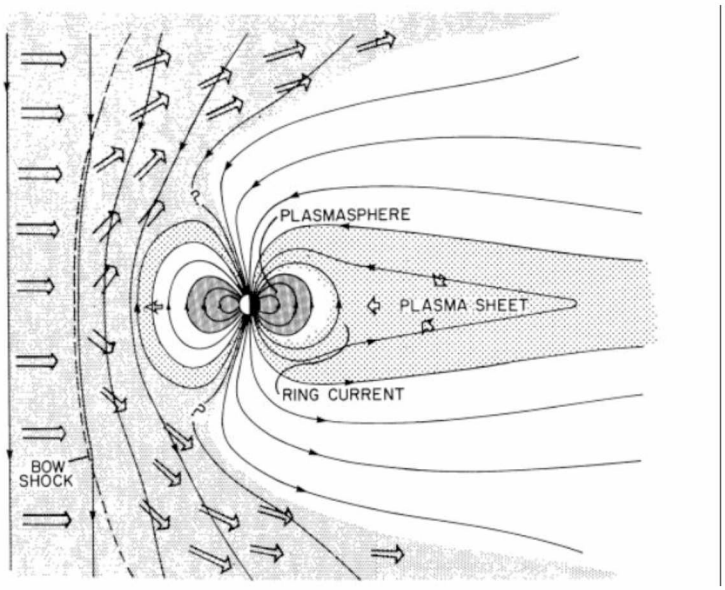

Figure 2: Solar wind incoming from the left interacting with the magnetosphere. Reconnection can be seen to the right of the plasmasphere, and it can be inferred how the magnetosphere deflects the solar wind, transferring the energy to the poles. Image from (*Wolf*, 1975)

Interaction between the solar wind on open field lines and the magnetosphere drives global magnetospheric convection. This coupling results in auroral field-aligned current systems and electron precipitation. By coupling the gradients of density, pressure, and magnetic field with shear Alfvén waves and magnetic reconnection, solutions to the kinetic Alfvén wave equations can be solved (*Johnson and Cheng*, 1997). It is partially through these kinetic equations that the naturally occurring interactions between the magnetosphere and the ionosphere can mathematically be coupled.

1.4 Contemporary Models

The contemporary models of the ionosphere and magnetosphere are varied in both accuracy and complexity. Simplistic models work on large scales within either the ionosphere or magnetosphere, however issues surface involving the coupling of the two systems. More realistic models account for some of these differences, but are bulky and lack spatial scale information necessary for accuracy as increased physics and wider computational domains limit computational resources and lower resolution. Transport models have shown accurate representation of M-I coupling and can be strengthened by filling in the missing parameters of spatial scales such as plasma density through this mission (*Lynch,* 2012).

When modeling big systems such as the ionosphere, simplistic models use steady state approximations, treating the system as a uniform passive sheet at the bottom of connecting flux tubes. More realistic models allow for different outputs of structuring and temporal response at different altitudes, changing bulk parameters (*Lysak,* 1999) with transmission and reflection of Poynting flux varying for different frequencies (*Lysak*, 1985; *Knudsen et al.,* 1990). Transport models show the difference of ionospheric response to hard and soft precipitation of electrons, such as the TRANSCAR model (*Lilensten and Blelly,* 2002).

An important part of magnetosphere-ionosphere coupling comes from the perpendicular E-field structuring of the ionosphere, demonstrating an ionospheric parameter. This is seen clearly in models such as TRANSCAR. The ionosphere is a large source of field-aligned currents, due to the horizontal structuring of $\boldsymbol{E}_\perp$ and conductivities. In terms of M-I coupling, the parallel current can be shown in the electrostatic limit to be (*Kelley,* 1989; *Brekke*, 1997):

$$J_{||} = -\Sigma_p(\nabla_\perp \cdot \boldsymbol{E}_\perp) - \nabla_\perp\Sigma_p \cdot \boldsymbol{E}_\perp + \nabla_\perp\Sigma_h \cdot (\boldsymbol{e_1} \times \boldsymbol{E}_\perp) \quad (4)$$

Where $\mathbf{e}_1$ is the unit vector along the geomagnetic field, Σ_p is the height-integrated Pedersen conductivity, and Σ_h is the height-integrated Hall conductivity. Because the field-aligned currents change the ionospheric conductivity through electron precipitation, allowing for conductivity gradients creates an ionospheric feedback mechanism (*St. Maurice et al.*, 1996; *de Boer et al.,* 2010; *Russell et al.,* 2010, 2013). If inductive effects are included, further instabilities arise (*Streltsov and Lotko,* 2008). With moderate conductivity and scale size, these generated currents show differences on the order of 5μA/m^2 (*Kelley,* 1989), and for finer structures the results are more dramatic. Because of this, determining these spatial scales is important in the understanding of magnetosphere-ionosphere coupling. Σ_p, Pedersen conductance, can be measured from electron precipitation (*Reiff*, 1984), and when included with Alfvénic coupling results in an ionospheric feedback effect which arises from current continuity (*Streltsov and Lotko,* 2008; *Cohen et al.,* 2013).

In more recent simulations, coupled thermosphere ionosphere models can be used, as well as the Open Global General Circulation Model (*Connor,* 2016). Similar approaches are being used to target other planetary bodies, such as Mars and Pluto, relying on physical parameters, ion-neutral chemistry, and radiative processes (*Bougher*, 2015). While there are many different models

that can be used to model ionosphere-magnetosphere interactions, the Gemini model is specifically targeted for this research study.

The Gemini model developed by *Zettergren and Semeter* (2012) has been used to interpret plasma density and thermal signatures. The model couples a two-dimensional five moment multi-fluid model (conservation of mass, momentum, and energy) of seven ionospheric species to an electrostatic treatment of auroral currents (*Lynch*, 2103). Having an arbitrarily adjustable scale size allows the model to be run on local or global scales, though resolution varies accordingly. The model uses inputs of either field-aligned currents or electric potential and precipitating electron fluxes, which vary spatially and temporally across the top boundary. For Isinglass these model inputs come from the in-situ rocket measurements as well as ground based instrumentation across Alaska such as PFISR and SDI's explained further in section 3.2. Wind fields can be additional inputs across the entire grid. By combining this model with PFISR measurements, allsky 427.8 mm data, and Scanning Doppler Imager (SDI) wind fields, electric fields inside the simulation domain, densities of all major ionospheric species, drift velocities, and temperatures of all major species can be calculated at most desired times and spatial resolutions. With this model, finer resolution shows current density at an order of magnitude higher than what coarser resolution can show, leading to a higher total current shown in these models. This means that there is unresolved specification on the spatial scale required for accurate results.

In order to gain an understanding of what is meant by gradient scale length, it is important to examine the need for determination. Figure 3 shows measurements from the Cascades Rocket, launched in 2009. It can be seen that the magnetic field data varies drastically and quickly over time, with spikes reminiscent of delta functions showing differences in different regions. When modeling such step functions, it is important to determine the cause for the spikes, be it plasma density, temperature, ion flow rate, or other such parameters. The scale length is the critical distance at which differences in these parameters can be observed, information that is necessary when modeling such processes.

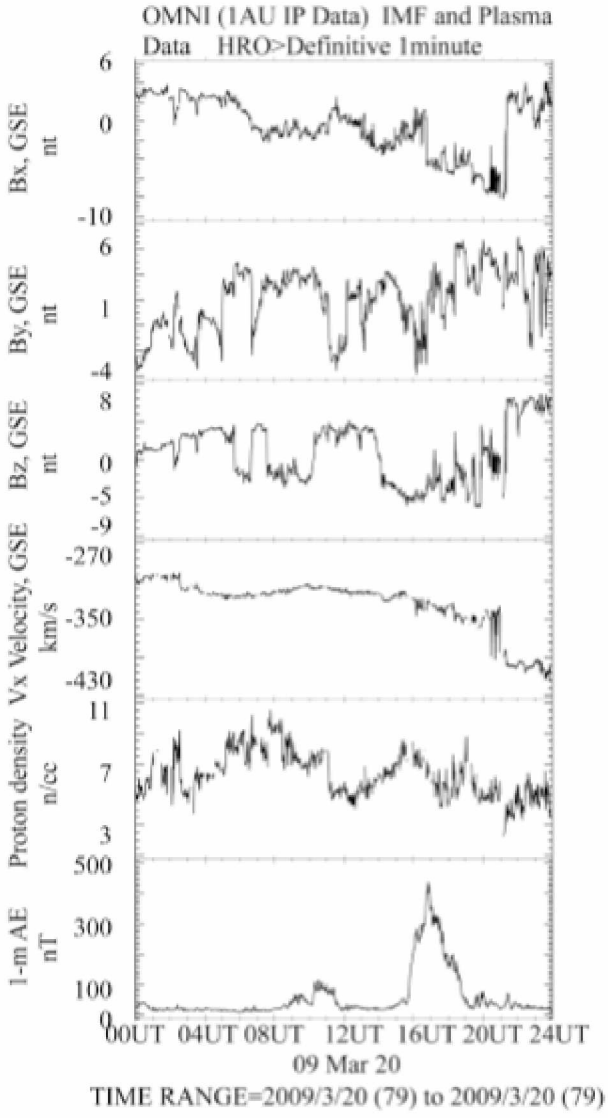

Figure 3: ACE (Advanced Composition Explorer) from CDAW Omni Website; 24h of 20 March 2009, Data providers are J.H.King and N. Papatashvilli at AdnetSystems, NASA GSFC and CDA Web., adapted from *Lynch et al.*, 2012.

Given the aforementioned parameters, ionospheric gradients matter to the understanding of coupling. In spite of this, no coordinated in-situ and ground-based observations of the gradient scale lengths of this structuring exist. The goal of ISINGLASS is to quantify these scales and quantify to what extent simulations such as *Zettergren and Semeter* (2012) accurately represent the effects of structuring on specific scales, yielding insight into the minimum scale sizes necessary for capturing significant M-I coupling effects (*Lynch,* 2013).

Chapter 2: Introduction, Goals

2.1 Goals of the Mission

ISINGLASS Goals

The primary goal of ISINGLASS was to see how the observed spatial scale lengths of ionospheric plasma structure is related to the characteristics of different auroral drivers. This was measured through a rocket launch and release of magnetometers and ion temperature sensors at different distances from the payload. By finding the trajectories of the sensors and meshing the data, differences were seen and sensitivity of scale lengths were evaluated. Further, the significance of the spatial scale lengths is being evaluated for how it affected magnetosphere-ionosphere coupling (*Lynch,* 2013).

NASA Goals

NASA's interest in the mission was the application to heliophysics and geospace, specifically how ionospheric forcing influences the ionosphere-thermosphere system's response to and regulation of magnetospheric forcing. The experimental model is also an important goal, testing how particle precipitation spatial gradients regulate ionosphere-thermosphere-magnetosphere dynamics by developing multipoint sensor array technology. A final goal was to measure and assess the significance of the spatial distributions of ion densities, one of the most poorly measured parameters of the IT system (*Lynch,* 2013).

Personal Goals

While I was not the PI on this project, there was still much I hoped to get out of the project. I would be part of an interesting research project and NASA rocket launch campaign. I would serve as an operator at an optical site downrange of the launch facility on the north side of the Brooks Range 150 miles into the arctic circle. Our group would examine whether using triangulation to reconstruct the relative locations of the launched objects through LED beacons and downrange optical sites was sufficiently accurate to answer the science question. I would install important instruments for the mission, both a spectrometer to assist the allsky at Toolik Field Station as well as a hard stop for the filter wheel for the SDI in order to solve a homing issue that made using the correct filter color difficult from long range. After the mission, I would test a program written by Mark Conde for triangulating the positions of upper atmosphere chemical releases, hoping to broaden the application of the program for later use.

2.2 Motivation

In the age of technology, many disciplines are using simulation in place of complicated or expensive experimentation. Because complex and numerous parameters often make rigorous experimentation impossible, atmospheric physics is at the forefront of these disciplines. In every case, the strength of the model lies in experimentation to find bulk parameters and relationships. In large-scale simulations, it is important to preserve the resolution of the model without using unnecessary computing time. Techniques have been developed to minimize this issue, defining specific parameters and using set scale lengths in order to turn a system of particles and interactions that is too large to count and track into a usable finite system that is free to interact.

Over the past 25 years, independent models of the middle ionosphere and upper magnetosphere have made progress. The physics of these layers is well understood, and it is possible to model these processes. The coupling between the two regions is what provides problems for models. The two layers are coupled through Ohm's law, current continuity, and particle kinetics (*Wolf*, 1975). Physicists feel they understand the underlying physics, however it is a complicated system, and therefore needs many complex equations to accurately model this coupling. In order to make an accurate model, it is important to incorporate many different parameters into the equations, such as magnetosphere and ionosphere electric field, field-aligned and perpendicular current, as well as particle pressure.

While simulations that exist consider these different processes, many models fail to capture the finest spatial and temporal scales that are needed to incorporate all relevant physics. The large and meso-scale models treat the plasma as a fluid, with meso-scale resolving ion inertial scale lengths, the scale at which ions decouple from electrons. The smallest scale used is the kinetic-scale, resolving dynamics down to the electron kinetic scale, showing the movements of electrons. Many thin arcs (1km) map to the electron inertial length in the acceleration region. These scales all have benefits and drawbacks, but while the kinetic scale resolves the model most accurately, it is computationally taxing. Because of this, finding a proper range of spatial scales of forcing for accurate representation of ionospheric parameters is necessary for merging magnetospheric and ionospheric models for magnetosphere-ionosphere coupling studies. Successful incorporation will

show whether scales that appear in localized high-resolution models match those that are actually observed.

The magnetosphere and ionosphere are coupled by the currents and Poynting flux that flow between them. As noted previously, horizontal structuring of these perpendicular ionospheric electric fields and conductivity makes the ionosphere a source of field-aligned currents. Since field-aligned currents change the ionospheric conductivity, this creates an ionospheric feedback mechanism. If inductive effects are included, instabilities arise. This is significant because these gradient-generated currents that arise are large even for moderate values of conductivity. For finer structures, the results from this feedback are much larger. Therefore, the size of these spatial gradients matters to our understanding of coupling, and almost no observation of specific gradient scale lengths exists, as radars cannot distinguish scale lengths at arc edges (*Lynch*, 2013).

The primary goal of ISINGLASS is to quantify these scales and compare to current models in order to assess their accuracy. This will give information as to the minimum scale sizes necessary for seeing the effects of magnetosphere-ionosphere coupling. Other goals of the mission are to test existing models, looking to what level of accuracy local ionospheric models properly simulate the response to different spatial structuring in the drivers and driving processes. In the response to the forcing, how important is the perpendicular structuring? The spatial gradient scale is most likely variable due to different auroral drivers, so the goal is to look at two different events and measure to what scale the spatial gradients matter.

It is important to have a good understanding of ionosphere-magnetosphere coupling because there are wide spread applications. Other than modeling our own system, there is likely similarity to other celestial bodies. In addition, lower ionosphere and thermal plasma studies have similarities to surface plasma studies necessary for laboratory and industrial plasma devices, and planetary dusty-plasma studies (*Lynch*, 2013).

2.3 Auroral Target

As outlined in the proposal, the goal was to sample two aurora events with significant characteristics. While substorm aurora contain inverted-V aurora, they are not a good choice for a rocket target due to their quick motion across the sky and short temporal scales. A quiet evening

arc is instead a good target for observing the effects of quasistatic aurora, as it often spans the sky for hours leading up to a substorm event, progressing toward the equator as the magnetotail loads. In spite of varied precipitation energy spectrum which occur with a large expanse of aurora (clear boundaries north-south and their wide expanse longitudinally), an evening arc is a good target for this study.

For the second target, an Alfvénic event was chosen. A rayed Alfvénic curtain during a poleward boundary intensification event presents as an easily identifiable Alfvénic event. Unlike quasistatic substorms, poleward boundary intensification events tend to remain at one location for up to several hours. Early evening arc source population is acceleration of plasma sheet electrons with magnetospheric source temperatures, while pole boundary intensification curtain source is the Alfvénic acceleration of cold ionospheric electrons excited by energy transfer from the equatorial magnetosphere to the ionosphere (*Lynch*, 2013). By launching into events that represent two general types of electron acceleration, structuring of the thermal ionospheric plasma can be examined to determine how the scale lengths compare for each type of acceleration.

Chapter 3: Methods, Hardware, Experimental Design

What follows is an overview of the methods used in the ISINGLASS mission, outlining both instruments and techniques used in the sky and on the ground. This information was first presented by Kristina Lynch in the original ISINGLASS proposal (*Lynch*, 2013), and uses the proposal and subsequent experiments for supporting information and understanding of the mission. The experimental design of the mission consisted of a rocket flight from Poker Flat Research Range (PFRR) as well as ground based instrumentation and field sites at Venetie, Coldfoot, Toolik Field Station, and Poker Flat, which provided images of the sub-payloads, as well as instrumentation at Poker, Homer, Toolik, and Kaktovic which provided auroral data. As part of ongoing analysis, this information is being incorporated into the subsequent modeling studies and fed into the ionospheric simulation for interpretation.

3.1 On Board Instrumentation

The rocket component of the mission consisted of two identical payloads launched on different dates from Poker Flat. Each rocket consisted of a three-stage Black Brant 10 rocket (Terrier/BBV/Nihka Combination) with instrumentation and sub-payloads (Figure 6). The main payload carries four instrumented sub-payloads (Bobs) and one COWBOY sub-payload which are ejected into a 5-point array in flight. Expected apogee was 350 km and expected downrange distance was 350 km.

On the main payload, the *Acute Precipitating Electron Spectrometer* (APES) was oriented along the magnetic field to record flux of auroral electrons in the 150 eV to 30 keV range. This was included to provide measurement of the small scale and fast motion of the auroral structure as well as energy dispersed features. By using a magnetic deflection system, the entire energy spectrum is sampled simultaneously, however this is only possible by using one look direction. A 100mm microchannel plate (MCP) detection system was used with 50 discrete anodes positioned logarithmically, providing good energy resolution (Figure 4). The magnetic field strength required (~240 Gauss) was easily attainable with commercially available magnets. The use of a yoke created a stray field of ~0.1 Gauss at 0.3 m but since it was a constant field it was calibrated out of the magnetometer measurements.

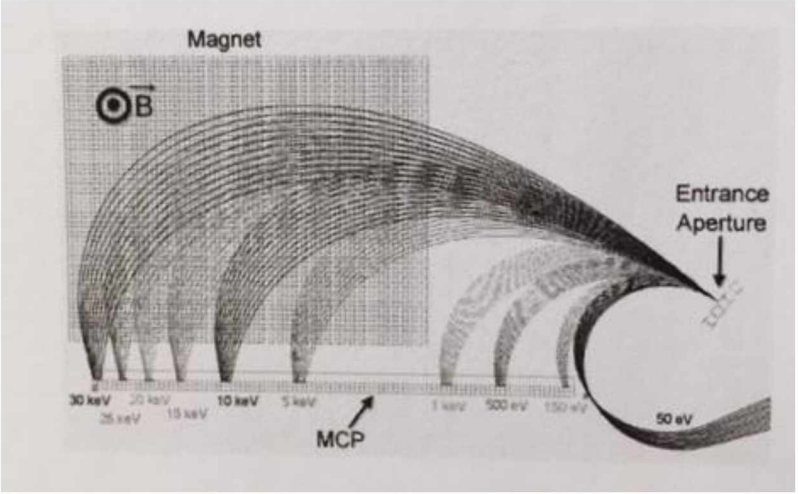

Figure 4: The Acute Precipitating Electron Spectrometer (Courtesy R Michell/M Samara)

The main payload carried five *Petite Ion Probes* (PIPs) and each deployed Bob carried two PIPs. The Bob is shown in Figure 5, below. Each PIP sensor is a cube approximately 1" on each side. The PIPs were developed at Dartmouth, and are a redesign of the NASA funded Dust Detector, a small Faraday-cup sensor designed for measuring mesospheric charged dust on tiny payloads (*Lynch et al.,* 2005*; Gelinas et al.,* 2005). The design was modified to measure the thermal ion population, providing three spatially separated, direction-sensitive measurements of the thermal ion distribution function, and some information about thermal electron temperature through current-voltage curve inflection point. The PIPs change the potential of their front screen and measure the resulting current. The relationship between current and voltage provides temperature and speed relative to the main payload. Thermal ion measurements can be used to look for variations in the plasma density, temperature, and flow. The flow vector was important since it provided an independent measure of the electric field by means of **E** x **B** drift.

The method developed for extracting plasma parameters from the PIP I-V curves includes realistic sheath physics. The analysis is done by modeling the sheath around the spacecraft using Spacecraft Plasma Interaction Software (*Guillemant et al.*, 2012, 2013). Once the potential structure around the spacecraft is modeled, a test-particle approach is used to quantify how the particles are perturbed by the sheath, and which ions make it to the detector. The particles which reach the detector are put through a model of the PIP in order to determine the I-V curve, giving a measurement of ion density, temperature, and plasma potential. The PIP is a low-resource sensor,

the low cost allows for many to be used in the analysis, providing more accurate data than one high-resource sensor, validated in the Cascades mission.

The main payload and the COWBOY sub-payload each carried an electrostatic retarding potential analyzer (ERPA), which characterizes the temperature of the ambient thermal electrons. Because the electron temperature is the dominant driver of the spacecraft float potential, the ERPA is valuable for interpreting the thermal ion measurements (*Siddiqui et al.*, 2011). An ERPA sensor is a cube with sides approximately 10 cm, and is a simplified Faraday cup with a retarding potential at the entrance for energy selection. The current collected by the anode is measured by a low noise electrometer circuit.

A fluxgate magnetometer was included on the main payload and the COWBOY sub-payload. These magnetometers have 16-bit sampling to measure field-aligned current (FAC) signatures (*Klatt et al.*, 2005). The magnetometer is a Billingsley three-axis fluxgate model TFM100. The main payload magnetometer was rigidly mounted near the center, far from possible disturbances, and the other one was mounted on the lower end plate of the COWBOY sub-payload.

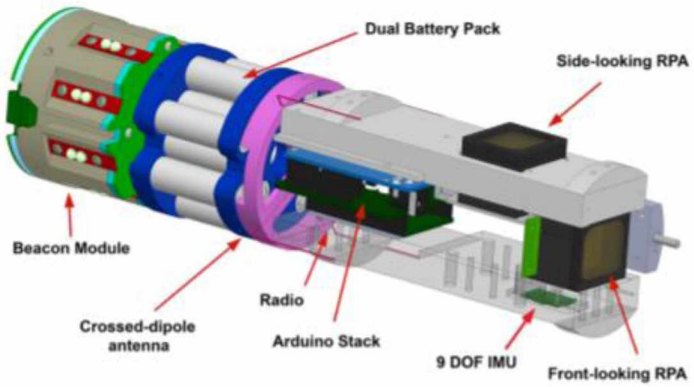

Figure 5: Bob used in the Isinglass Experiment (Courtesy Max Roberts, Kristina Lynch)

Each Bob (Figure 5) is a cylinder 11.5" long with 3.4" diameter. On each, there were two Petite Ion Probes (PIPs) that measured the thermal ion population. Each Bob also carried a small fluxgate magnetometer to determine Bob orientation, and was equipped with an LED beacon and accelerometer for use in determining the trajectories of each Bob. Each beacon consisted of battery powered LEDs which pulsed at a unique frequency for identification. The use of a GPS for

trajectory would have been preferable, but the Bobs are battery powered, and a 2 W GPS would have drained the batteries too quickly. On board, there was also a battery pack power source, a processor, and an antenna for sending data to the main payload for transmission to the ground. Since the Bobs were small, air resistance can be neglected and the fit extrapolated so that the LED beacons could be turned off while the instruments on them were collecting data so that the drive current for the LEDs would not contaminate altitude magnetometer data.

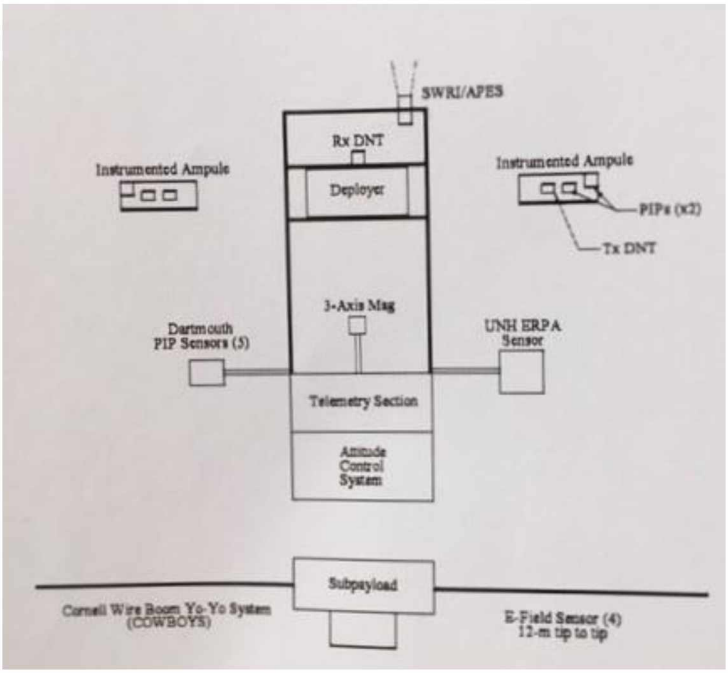

Figure 6: Schematic of the Scientific Payloads (Courtesy ISINGLASS Team)

The COWBOY sub-payload consists of orthogonal wire booms with a sphere at each end. Since this becomes a dipole antenna, as it spins, the amplitude of the electrical potential between the ends of the wires serve as an electric field measurement. By wrapping the wires around a cylinder and attaching them to the main payload through a spooling mechanism using magnetic damping, the device can un-spool without tangling or rewrapping in order to maintain feedback control. The electric field data measured with the COWBOY boom system are such that, when coupled with the pip output data in the Bobs, shears and gradients can be measured twice: over the 30 meter rocket as well as over the kilometer scale of the Bob-rocket system (*Lundberg et al.*, 2011). In addition, a small conductive disc was added to both the COWBOY and the main payload to serve as a fixed Langmuir probe for relative plasma density measurements.

3.2 Ground-based Instrumentation

Ground imaging was used primarily to characterize auroral events. By measuring red and green light emissions, the energy and flux of the precipitating electrons could be quantified in order to characterize the auroral activity prior to, during, and after the ISINGLASS payloads passed through the auroral event. The primary instruments were electron multiplying, charged coupled device (EMCCD) cameras that can collect digital data at 30 frames per second with a spatial scale of about 140 meters per pixel when observing at magnetic zenith. The primary site for camera placement was the village of Venetie, AK (67.019°N, 146.425°W), as the nominal rocket trajectory apogee would occur over Venetie at magnetic zenith.

A wide angle camera was fielded at Venetie to provide context images and observe the flashing beacons on the Bobs. Similar cameras were placed at Poker Flat (65.1367°N, 147.4472°W), Coldfoot (67.251°N, 150.175°W), and at Toolik Field Station (68.626°N, 149.596°W). These sites were chosen due to their geometric positioning with respect to nominal flight path and accessibility, with all except for Venetie being accessible by roads. All three down-range sites had ranges of less than 300 km to the rocket throughout the nominal trajectory. The camera operators were careful to orient themselves such that the Beacons were in the field of view of their camera, and that each image was timestamped correctly. At Venetie and Coldfoot, identical Sony Alpha 7 Cameras were used with lenses of 50mm at Coldfoot and 35mm at Venetie. At Poker, a Canon ME20 was used with a 50 mm lens. At Toolik, a Nikon D810 was used with a 50mm lens. While the field of view was slightly different for geometric reasons for each camera, the resulting triangulation resolution from each camera was about 0.5 km.

Observation from other ground-based instrumentation was used to further characterize auroral conditions. A 30 MHz coherent scatter radar imager was deployed near Homer, Alaska, extending well into the proposed rocket flight. From the images of radar echoes from waves in the auroral E region, estimates of the convection speed and direction were derived, producing regional pictures of auroral-zone electrodynamics. The groundbased Fabry Perot Network is a web of Scanning Doppler Imagers (SDIs) located at Eagle, Poker Flat, Toolik, and Kaktovik. Each SDI measures airglow spectra across a wide field of view in the sky (*Conde and Smith,* 1998). Using

the SDI data, an overlay of the data with allsky cameras and PFISR measurements provided a map of wind and temperature data at different spatial resolutions and different altitudes (See Figure 7). Spectra from individual SDIs directly measure the line-of-sight component of the vector wind field. These measurements can be inverted to give a spatially extended map of the horizontal vector field (*Conde and Smith*, 1998), so the array was to reduce assumptions with the inversion, give more detailed measurements, and (with uncertainty) determine the winds in the vicinity of the rocket flight.

Lastly, the Poker Flat Incoherent Scatter Radar (PFISR) provided both 2D large-scale electron density and line of sight plasma flow, from which electric field maps and volumetric conductivity structures were inferred. The electric field data was used to characterize auroral activity and the conductivities described in sections 1.2 and 1.3 and allowed for an independent check of the model results through comparison of measured densities. One particularly useful parameter that was found in this way is the parallel component of the current, described by equation 4 and indirectly inferred through modeling.

$$J_{||} = -\Sigma_p(\nabla_\perp \cdot \boldsymbol{E}_\perp) - \nabla_\perp\Sigma_p \cdot \boldsymbol{E}_\perp + \nabla_\perp\Sigma_h \cdot (\boldsymbol{e_1} \times \boldsymbol{E}_\perp) \quad (4)$$

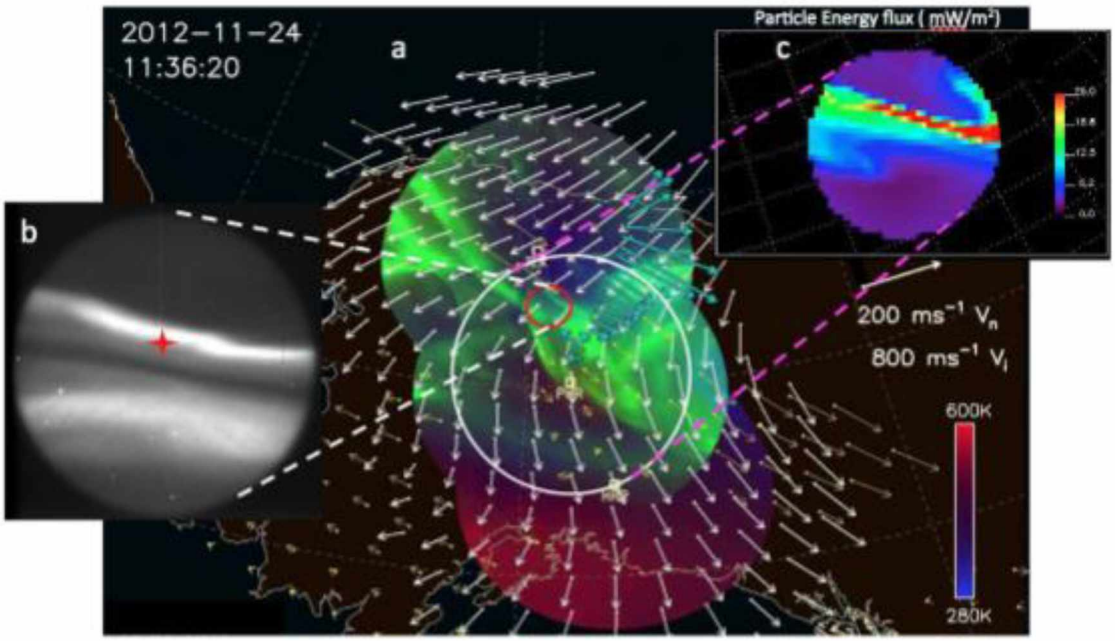

Figure 7: Wind field plot generated from assimilated data. **(a)** Green line emissions from allsky cameras, and E-region temperature maps obtained by Scanning Doppler Imagers (SDIs). F-neutral winds obtained by SDIs, ion convection from SuperDARN and PFISR. **(b)** Image from filtered Field of View cameras at Venetie. **(c)** Particle energy flux from SDI temperature map. Courtesy Hampton/Conde.

The launches were called using the extensive array of real-time data available at the Science Operations Center at Poker Flat Research Range. The proposed launch criteria were clear and specific: a quiet evening discrete inverted-V arc, and a poleward boundary intensification event (Alfvénic curtain). The window was chosen to minimize the moon, as this is important for optical auroral observations as well as to see the beacons clearly. Fortunately, in the launch window the solar cycle was far from solar minimum.

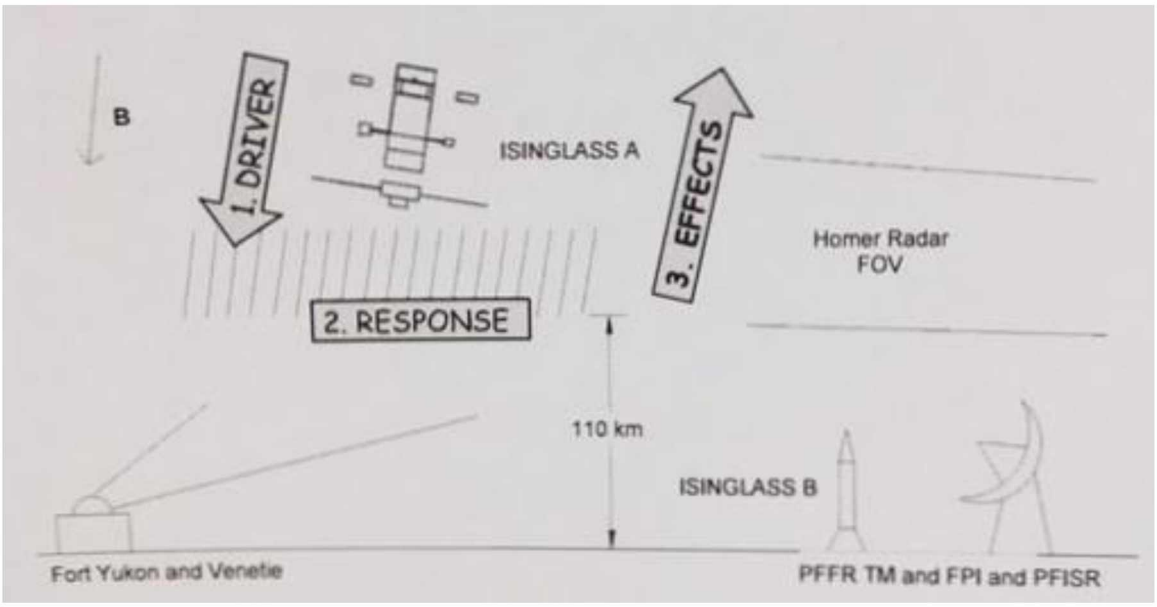

Figure 8: Schematic of the ISINGLASS mission illustrating tools for characterization, quantification, and evaluation of the underlying physics (Courtesy of K Lynch and Isinglass team)

Chapter 4: My Role in Isinglass

During the ISINGLASS mission, my role was to serve as an operator at an optical site at Toolik Field Station. Equipped with a Nikon D810 camera, my primary responsibility while in Toolik was to take a series of images at a predetermined frame rate from Toolik during the rocket flight.

4.1 In the Field

My primary objective was to obtain optical data from Toolik Field Station of the two Isinglass rocket launches in which the beacons were clearly distinguishable. The optical data consist of images that included the flashing LED beacons on the Bobs. The data obtained at Toolik and three other field sites would be analyzed in order to determine the trajectories of the Bobs relative to the main payload.

The look angle for my camera was chosen to improve the chance that the beacons on the Bobs would be seen in the images with enough resolution to observe each Bob separately. Since the rockets are purely ballistic, they are subject to a wide set of forces that can change the planned trajectory, such as wind and rocket motor performance. Because of this uncertainty, variations in flight path were anticipated and look angles were calculated for five different cases, shown in Table 1. The true trajectory of the rocket would be known after two minutes of flight, at which point the pre-calculated look angles for each case could be implemented with enough time to collect data.

	Azimuth (Geo)	Elevation	Azimuth (Mag)	Adjusted Az
Nominal	142.9°	48.8°	124.9°	15’40”
High-Short	155.0°	46.2°	137.0°	14’52”
Left	161.9°	53.3°	143.9°	14’24”
Low-Long	120.1°	48.4°	102.1°	17’12”
Right	129.8°	41.9°	111.8°	16’33”

Table 1: Given Azimuth and Elevation data for different rocket trajectories. Converted Azimuth is in the third column and Adjusted azimuth is on the right (Astronomical mount scale).

Because of the different possible trajectories of the rocket, it was vital to have a camera setup for which the look angle could be changed quickly and accurately. I used a tripod originally designed for telescopes equipped with a custom camera mount. This tripod had dials that represented the elevation and azimuth of the view. It is important to note here that while elevation (declination) was measured in a standard way on these dials, azimuth was marked in the astronomical scale, using hours and minutes instead of degrees. While the conversion is straightforward (1hr = 15°), conventionally the directionality of it is opposite, so for every angle given, calculations had to be made to turn azimuth into hours/minutes. The product of these calculations is shown in Table 1 above, and the calculations were done explicitly using:

$$Equivalent\ Reading\ on\ Mount\ (hours) = \frac{360° - azimuth\ (°)}{15°} \quad (5)$$

While the camera was unable to be outside for long periods of time due to the harsh conditions at Toolik, the tripod was able to stay outside in position. The metal mount designed for the camera had an easy release, meaning, once calibrated and positioned, the camera could be attached and aligned within ~20 seconds. This meant that it was only vital to orient the mount once during my month long stay. It was important to verify the position had not changed after harsh windstorms and on likely launch nights, but because the tripod was buried well, the position did not change. Initially there was worry that the harsh weather would freeze up the dials and the tripod would be unable to turn or rise/fall. Because we arrived three days prior to the launch window I was able to test this immediately, and even at -30° Fahrenheit the dials still turned fluidly and registered the correct position.

In order to orient the mount, it was first important to find true north. Because Toolik is at 68.626 degrees latitude and not along the longitude of magnetic north, the difference between true north and geomagnetic north is substantial. By consulting google maps as well as a compass, I was able to ascertain that there was an 18° difference between true north and magnetic north. Checking the alignment both with maps and landmarks as well as this 18° difference using a compass, the tripod was successfully set so that 0 hours faced true geographic north. The elevation was set using a level on top of the metal camera attachment and then the tripod was buried with about one foot of snow, as seen in Figure 9. In order to confirm the alignment, I set up the camera and took test images at specific azimuth and elevations, which were verified by comparing stars in the camera

image to star charts. The tolerance of these measurements was forgiving because as long as the beacons were visible in the images it would be possible to orient them against the stars.

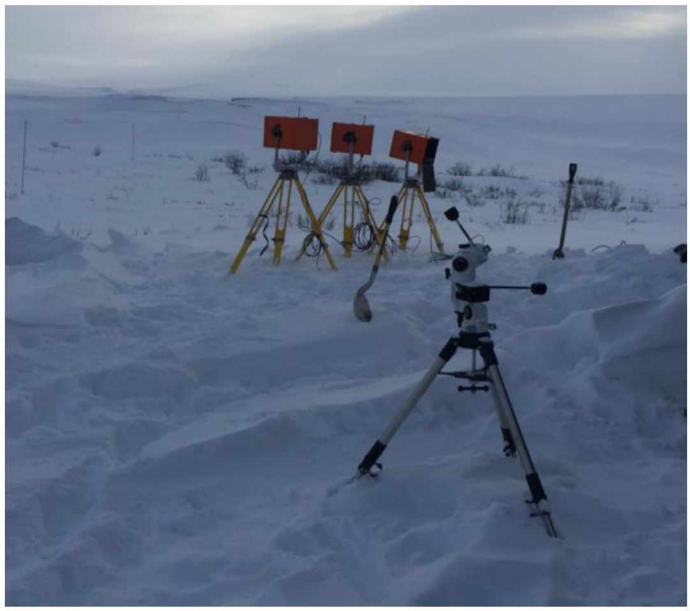

Figure 9: The astronomical mount in the foreground is my setup, buried in about a foot of snow. The three cameras in the background are Clemson's setup, for capturing Trimethyl Methyl Aluminum release.

While the field of view for a 50mm lens on the Nikon D810 was much larger than the projected spread of the beacons, it was important to change the camera to the correct look angle after two minutes of flight. In order to do this quickly, there had to be good communication between the different field sites, accomplished through Skype. For a full timeline of each launch, see Appendix I at the end of this document.

In order for the post processing of the images and determination of the trajectories of the Bobs, it was necessary that the timing of the images be known to within 1/30 of a second for each site. For Venetie and Coldfoot, identical equipment allowed setting the frame rate to 1/30 of a second at each site, making it possible to reduce the uncertainty in the eventual calculations to within 1/60 of a second when calculating the trajectories of the rockets. Inclusion of different frame rates at Poker and Toolik increased uncertainty slightly, however since the data still fell within 1/30 of a second, it was valid and useful. Because the images needed to be synchronized in order to calculate the trajectories, it was important to time-stamp the images. At Toolik, the absolute timing was accomplished through a GPS receiver that set the camera time. At Venetie, Coldfoot,

and Poker, an audio record of an operator specifying the approximate time was relied upon, and the absolute time was set when first light was seen in the beacons, giving uncertainties of 0.25 to 0.5 seconds. Relative timing between Venetie and Coldfoot was accomplished by looking at what time the beacons came on, and it was found that the timing was off by about $1/60^{th}$ of a second.

4.2 After the Mission

After the mission, I collected the optical data from Poker, Venetie and Coldfoot in order to calculate the trajectories of the Bobs. Toolik was clouded during launch so collected data was not used for analysis. Because the hardware used at Venetie and Coldfoot were identical SONY Alpha 7S's, a quick comparison and calculation was possible to find the locations of the beacons using existing software by Hans Nielson (See Figure 13). The Canon ME20 digital CMOS camera operated at Poker Flats provided a third optical site. My role was to create a trajectory using the third site and compare the results to the previous calculation. While this fit seemed accurate on first glance, the third site decreased overall uncertainty of the fits and helped to answer the research question when compared to data from onboard instruments.

In order to make the fits, I used "Skytracker" software written in Interactive Data Language (IDL), a coding language, by Mark Conde. The software was initially developed for use with upper atmospheric chemical releases to track the motion to determine atmospheric winds; however, the use for calculating trajectories of the Bobs was similar. The software works by taking different look angles of cameras and GPS locations in order to project a starmap on an image. In theory, this is straightforward, however the look angles map in a nonlinear way across the image, meaning that more work must be done in order to align the stars in the image with the starmap.

In order to make a connection between the image and the starmap, the user must accurately map the stars to the image (Figure 10a). The software uses geoid reference W-GS 2000 and projects the Harvard Bright Sky Catalog on the camera image using the GPS coordinates of each site and UT timestamps for each image. By performing a geometric calculation using the lens specification and pixel size, it was found that the smallest angle subtense of a pixel (Nikon D810) was 0.00098 radians. Because at the celestial equator the stars would have shifted 0.00291 radians in 40 seconds, the change in star position in celestial coordinates (RA and Dec) is negligible over the short timescale in which images were taken, with stars moving only 3 pixels. This is an

overestimation, as the images were taken far north, and the other cameras had an angle subtense that was larger (See Table 2 below). This subtense is also negligible compared to the separation of the Bobs, which are separated by about 500 pixels in high definition images. In spite of this, the altitude-azimuth coordinates of the images are predicted. This means that when the image from a camera is projected on the dome, there is an obvious discrepancy between the location on the image and the starmap of these bright stars. It is then up to the user to accurately assign the starmap to pixel addreses in the camera image in the vicinity of the Bobs, allowing for camera look direction, rotation, magnification, and lens distortion.

Camera Site	Focal Length	Pixel Length	Camera Type	Angle Subtense (rad)
Venetie	35 mm	8.5 μm	Sony A7	0.00243
Coldfoot	50 mm	8.5 μm	Sony A7	0.00170
Poker	50 mm	19 μm	Canon ME20	0.00380
Toolik	50 mm	4.9 μm	Nikon D810	0.000980

Table 2: Angle Subtense of a pixel in each image calculated using $\tan^{-1}(\frac{pixel\ length}{focal\ length})$.

Once connections have been made (Figure 10b) from the stars in the image to the markers in the catalog, it is possible to map the 2D image onto the dome. When the user targets the positions of the beacons (Figure 11), the interface preserves information about azimuth and elevation for the target image, and creates a ray in space where the location is at this point of time. When more than one temporally synchronous image has been processed in this way, the geodetic position of the target in 3D space can be calculated.

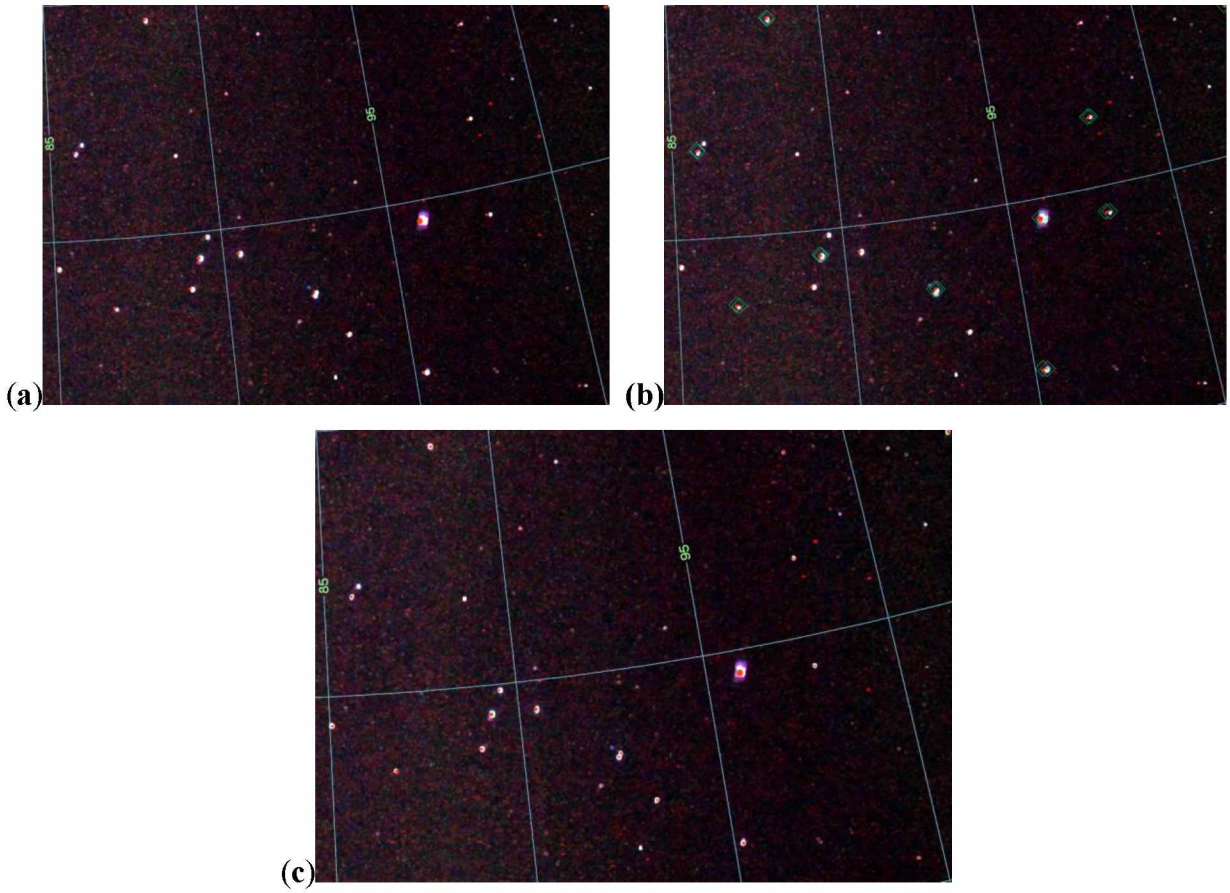

Figure 10: Geoid projection places red dots in the location of bright stars. It is up to the user to connect the stars in the image to the dots from the program. Once connections have been made, the program warps the image. The images above represent an unmapped (a) image with connections made using the Skytracker program (b) and the final mapped image (c).

When simultaneous images are analyzed from different sites (i.e. Venetie and Coldfoot), rays are created from each optical site to the Bob and ideally the intersection point of multiple rays would be the location of the target (Figure 12). Due to errors, the rays rarely intersect exactly. The software calculates the 3D location of the point in space that minimizes the miss distances between each ray. Using more than two sites strengthens the results assuming careful identification. Because the beacons were turned on for ~40 seconds, this provided a sufficient amount of data, from which a fit could be determined.

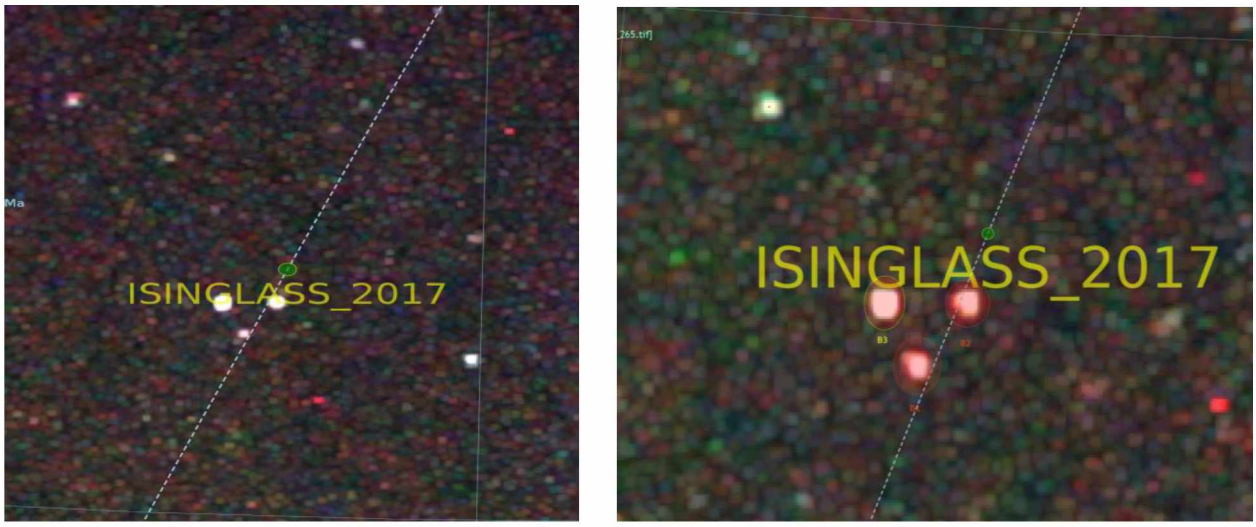

Figure 11: Once the image is fit to the starmap, targets can be identified as specific beacons. The triangle of dots are the beacons, and the green dot represents the rocket. The image on the left shows the beacons clearly visible with the main payload position represented by the dotted line, while the image on the right shows identified beacons. The yellow ellipses identify each target, the red ellipses indicate uncertainty, and the text underneath names each target.

There were four Bobs, however the beacon on one of the Bobs did not turn on, so there were three distinct points in the sky in addition to the fixed star points. In order to differentiate the individual Bobs, each beacon was programmed with a different flash frequency: 1.0 Hz, 1.3 Hz, 1.6 Hz, and 1.9 Hz (See Figure 13). The 1.6 Hz beacon did not turn on. Because each image was time stamped accurately, this gave a clear method of identification. Geometrically, each Bob was far enough apart so that each beacon was a distinct point, and by analyzing images at different sites, individual Bobs could be distinguished. Venetie and Coldfoot had geometrically beneficial relationships to the rocket, displaying chiral opposites of each other (Figure 13), while two of the beacons overlapped in the Poker view geometry (Figure 14). By analyzing the time difference as well as a slight separation between the beacons, it was possible to distinguish all the Bobs.

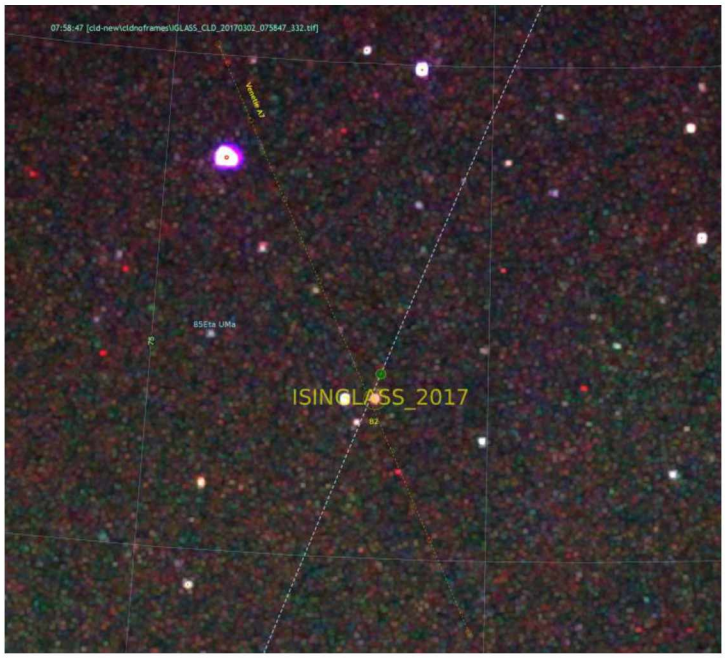

Figure 12: Identification and Subsequent ray tracing analysis outputs position information in the form of geodetic longitude, latitude, and altitude. The yellow ray (top left to bottom right) represents trajectory of the highlighted Bob from Venetie, and the white ray (bottom left to top right) is the trajectory of the main payload.

It is important when calculating these trajectories to find enough intersecting points to reduce error and track the trajectory when the beacons were on, about one every 5 seconds. To find the error, the program uses visual uncertainty parameters. Specifically, the target is located by the programmer and marked by drawing an ellipse around the target centered on the target. The uncertainty is found in a similar way and marked by drawing a smaller ellipse around the point of light itself. Figure 14 shows this marking in progress, with B2 properly marked and B1 in the process of being marked. To calculate the uncertainty, the program uses a monte carlo algorithm to solve for the position in 256 random points within this ellipse and does a subsequent standard deviation calculation on the answers in order to calculate the error.

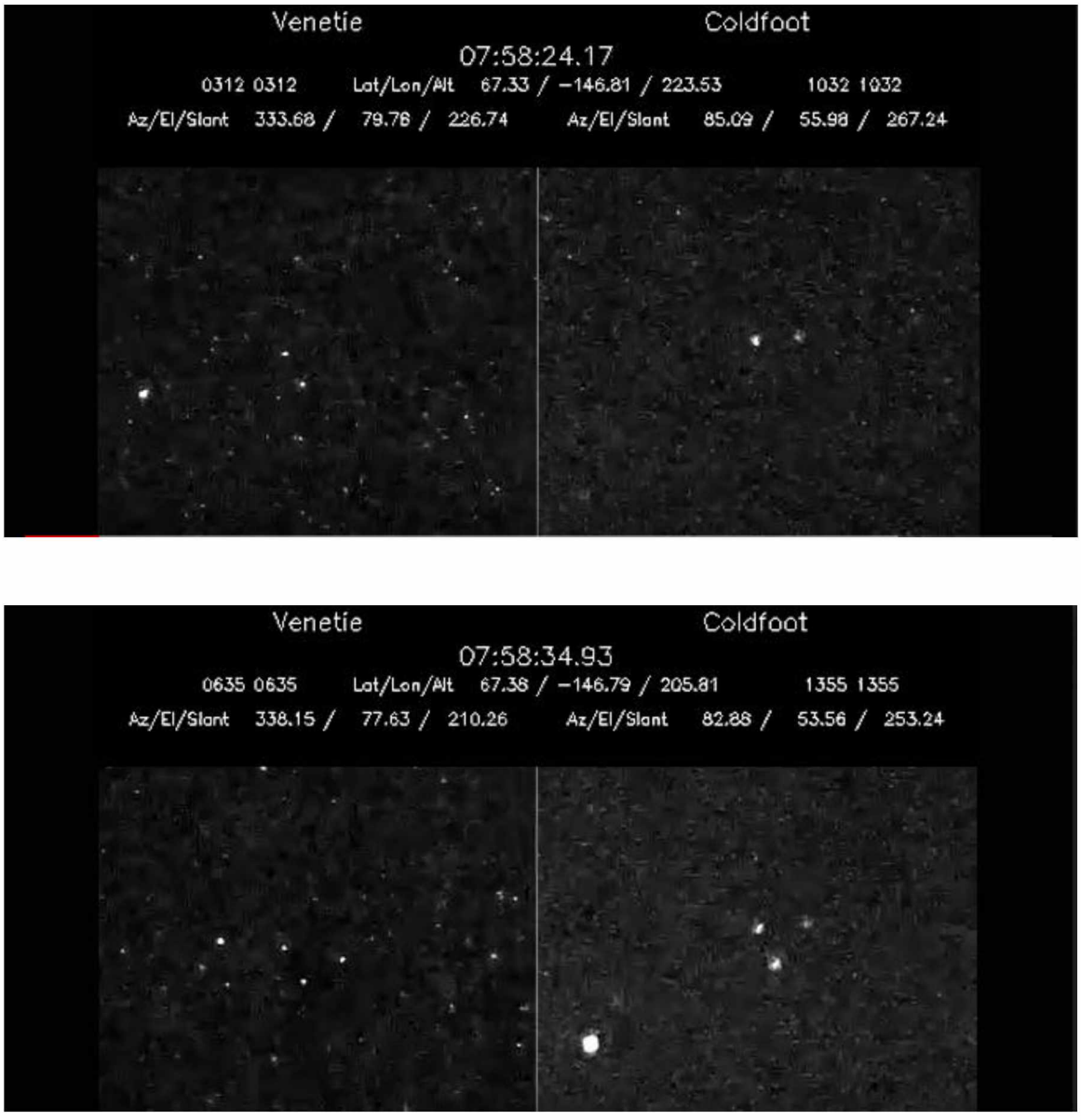

Figure 13: The two stills above taken from a .mp4 of the initial Bob trajectories shows the positioning of the Bobs as seen from Venetie and Coldfoot. The frequency difference is represented by the two beacons visible in the upper image and the three beacons visible in the lower image.

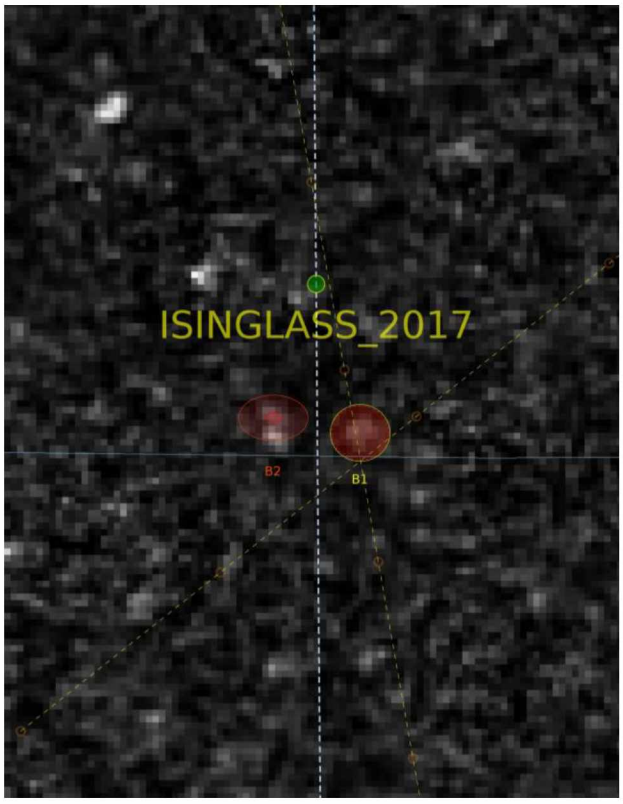

Figure 14: The image above is one of the poker images. B1 and B2 are clearly visible, with B3 appearing directly underneath B2, not yet marked in this image. This image is in the process of being marked for uncertainties, with the red ellipse showing the uncertainty.

4.3 Supplemental Responsibilities

Supplemental responsibilities during the mission were troubleshooting and fixing an issue with filter alignment and calibration with an SDI, installing a hard-stop for the filter wheel on the SDI, and managing the technology of both the SDI and spectrometer at Toolik Field Station. Other responsibilities directly related to the mission included multiple reports per day on weather and conditions, installing a spectrometer in the 'smurf hut', and being in constant communication with the rocket range over the course of the mission while standing by for acceptable auroral conditions.

I went to Toolik a week before the launch window opened with two colleagues to diagnose poor data being output by the SDI prior to the mission. The problem seemed to be a homing issue with the filter wheel. The SDI filter wheel consists of six places for filters, and contained both a red and green filter which allowed for wind data to be taken at two independent wavelengths. This left four empty spaces. Because the device loses power when Toolik loses power, if the filter wheel

is misaligned, it does not know how to home. Due to this issue, the data had recently been poor, sometimes not going through a filter at all. At this point, I returned to UAF with the knowledge necessary to prepare for the window.

I arrived at Toolik a few days before the window opened so that I would be able to prepare for data collection and rectify the issue with the filter wheel. I came equipped with a hard stop designed by the machine shop at UAF to fit into an open spot on the filter wheel, as well as a modified cap which served as a catch. Because of the strength of the catch to the motor, once caught, the filter wheel would not turn. This would serve as the new 'home' for the wheel so that the SDI, as well as the operator back in Fairbanks could be assured of the position. Installing the wheel was difficult, as access to the filter wheel was only available from outside of the unit where it was housed. -30°F temperatures and high winds made working with metal more difficult. Once the filter wheel was installed all that remained was to write a script which homed the device and the problem was solved.

I installed a spectrometer in the same observatory to be used in the mission. Sent with the device and a computer to connect it, this was an easier task as it was installed from inside the trailer, and there was an available dome next to the preexisting allsky camera. The major difficulty at this point was alignment; however, through consultation with Don Hampton at UAF this was accomplished. Once connected, I set up the computer to be remotely accessed from Fairbanks. One of my most common supplemental responsibilities was to restart the computer connected to the spectrometer, as it disconnected frequently.

Chapter 5: Discussion/Results

During the 5 week window, two rockets were launched and data were acquired for each. Because of an issue with the sub-payload doors, discussed below, only one set of optical beacon data was acquired. In spite of this, useful data was retrieved from both launches.

5.1 Issues with Launches and Accommodations Made

In most scientific endeavors, nothing goes completely according to plan. In this mission, there were a few big problems that arose, one potentially devastating to the science involved. The proposed experiment consisted of two launches, probing two different experimental conditions, varying spatial gradients and auroral parameters. As mentioned above, this meant that the two different launches could show varying spatial gradients for different auroral conditions, potentially indicating a spatial gradient scale, answering the science question.

In theory, this makes sense, but in practice these are very expensive tests and if one does not work, it cannot be repeated for another year. The design was such that before the rocket hit apogee (highest point), a hinged door would open on the rocket, and springs would push the four Bobs in different directions. Unfortunately, there were problems with the first rocket; the sliding door did not open and the APES sensor malfunctioned. While there were still many other instruments on the rocket to collect data, our group was disappointed because now there was not as much data to compare when we did a second launch.

In designing the second launch, it was important that the mishap in the first launch was addressed. In this case, the goal was to ensure that the sub-payload ejection system functioned properly, addressing the wiring issues with the first launch. Only after confirming that the system functioned well was the launch sanctioned.

In order to try to minimize the uncertainty in the calculations, four optical sites were used, knowing that we needed at least two good data sets, and three would be preferable. Four would be ideal but due to the vast nature of Alaska and the variation in weather (not to mention the weather generated by the Brooks Range), it was improbable that there would be four useful sets of data.

Unfortunately, the issue with the door in the first launch made Bob data of little value. In spite of this, the onboard magnetometers and thermal ion density readers (PIPs) still took data that could be useful after calculating the second data set. Thankfully, for the second launch, good weather conditions remained at three of the sites so the launch went as planned. Toolik was clouded in, but all launch conditions were met. This launch was successful, with the door opening smoothly and almost all instruments operating as designed. The only issue was that one of the LED beacons failed to turn on, so only three of the four pips were trackable by our method. After triangulation and subsequent calculation, it was possible to infer where the fourth pip was through the spread of the Bobs as well as through accelerometer data. Unfortunately, this inference is not verifiable.

While the target auroral activity was to launch into two different auroral forms; quasistatic and Alfvénic, the limitations of the launch made it important to launch into a mostly quasistatic event twice. Thankfully, in spite of the auroral activity being predominantly quasistatic, there is a combination of both components of aurora in most auroral activity. This means that in both launches there were aspects of both quasistatic aurora and Alfvénic aurora, making the data from the launches useful across the spectrum of auroral and ionospheric physics.

5.2 Triangulation of Bob Position

Using the methods described in Chapter 4, position data was determined for the Bobs in the second launch. By finding the targets at many points throughout the 35 second beacon window, position data could be created from the output of the file (see Appendix II for the position file output). Using this data, plots of altitude and latitude/longitude could be created for each Bob (Figure 15, 16). While there was an issue with some of the velocity calculations, velocity data could be approximated from the separation data (Figure 17).

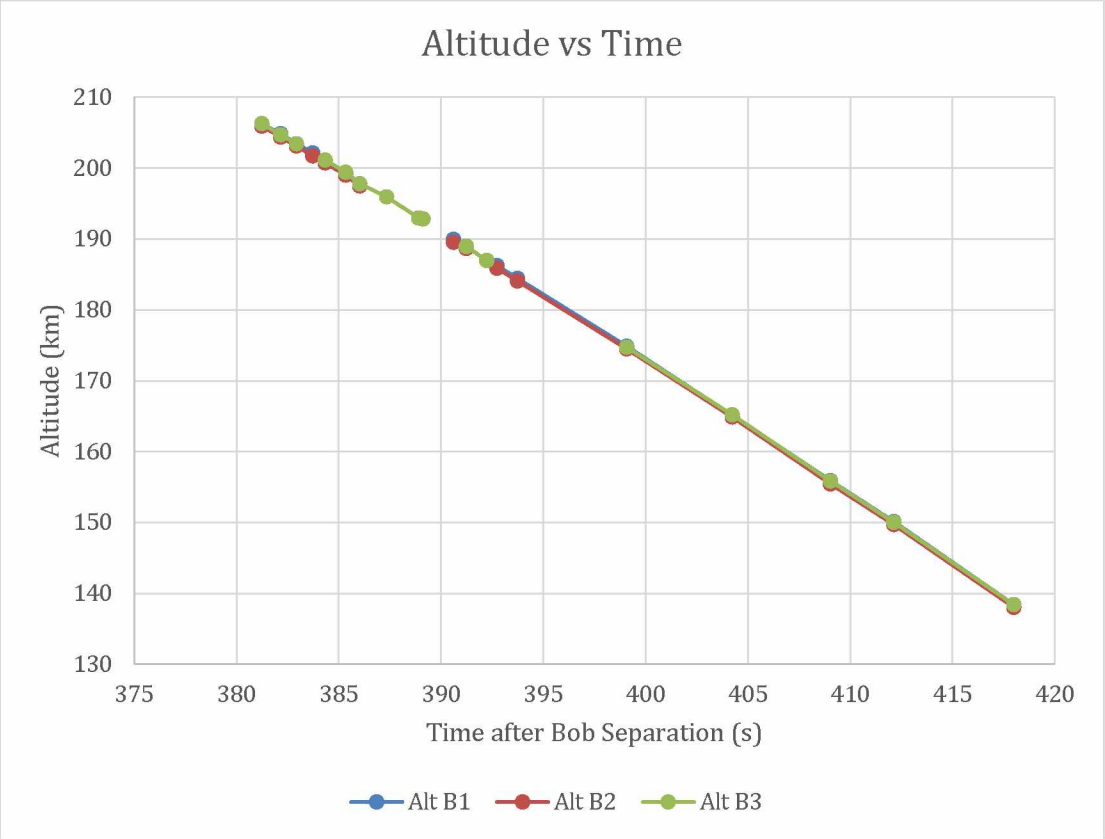

Figure 15: Altitude data of each Bob versus time calculated using the output shown in Appendix II.

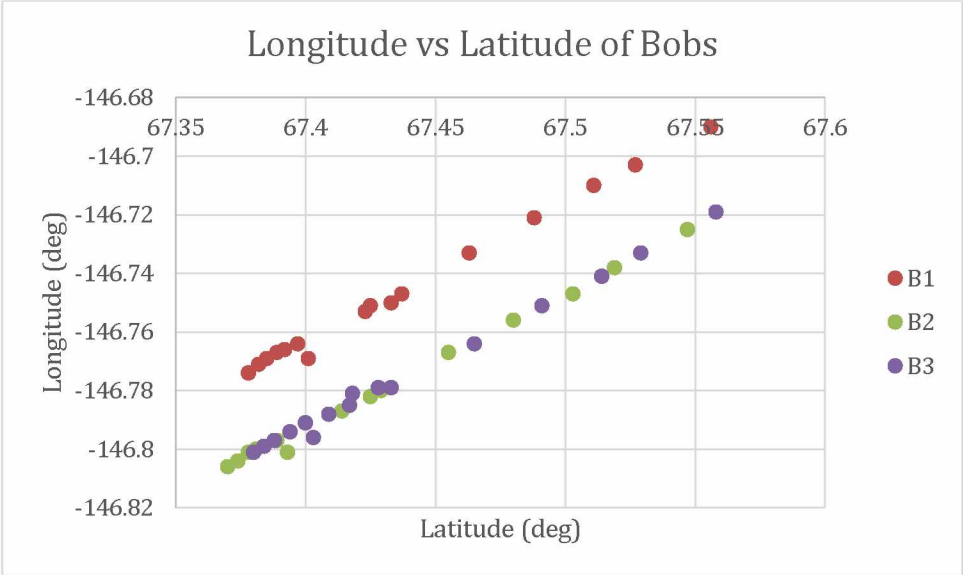

Figure 16: Latitude vs Longitude data for each Bob. Calculated using output from Appendix II.

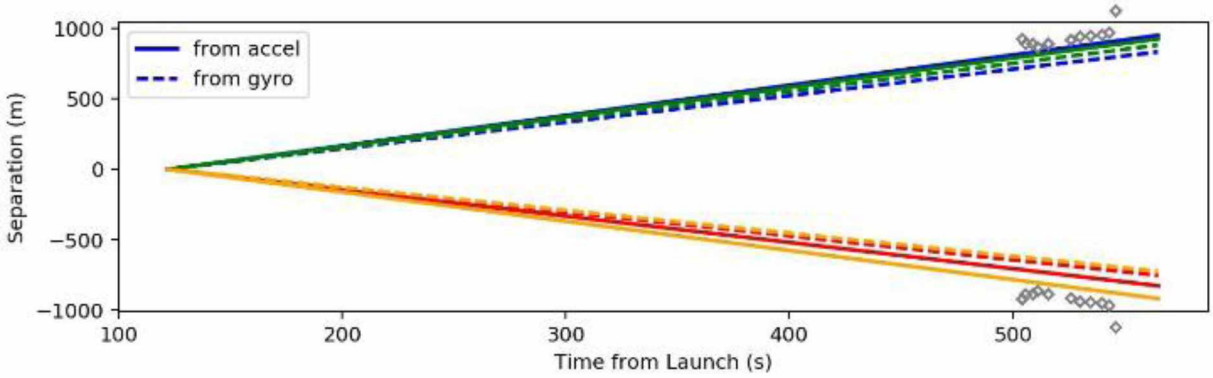

Figure 17: These plots show separation of the Bobs from the main payload, with data from accelerometer, gyro, and initial calculations done by Hans Nielson plotted together (Courtesy Donald Hampton and Hans Nielson)

The main issue with the calculated velocity data is that the calculations required to resolve velocity involve uncertainty propagation in such a way as to make the output statistically insignificant, as shown in section 5.3, below. The trajectory of each individual Bob is important, however the important quantity we are looking for is relative velocity between the Bobs, as it is their relationships to each other that will indicate a critical spatial scale. In spite of this, it is possible to gain a rough understanding of the velocity data of each Bob using the position and temporal data calculated using the program as well as the timing of the ejection of the Bobs. Because the position and velocity of the main payload is well known, one output of the program file (Appendix II) is distance from the main payload. Using this data as well as the timestamp, a plot of distance from the main vs time from launch could be generated for each Bob, the slope of which is the relative velocity of each Bob to the rocket (km/s). The resulting data sets can be seen in Figure 18 below. This calculation can be contrasted with an alternative computational source, created by Hans Nielson, and shown in Figure 17.

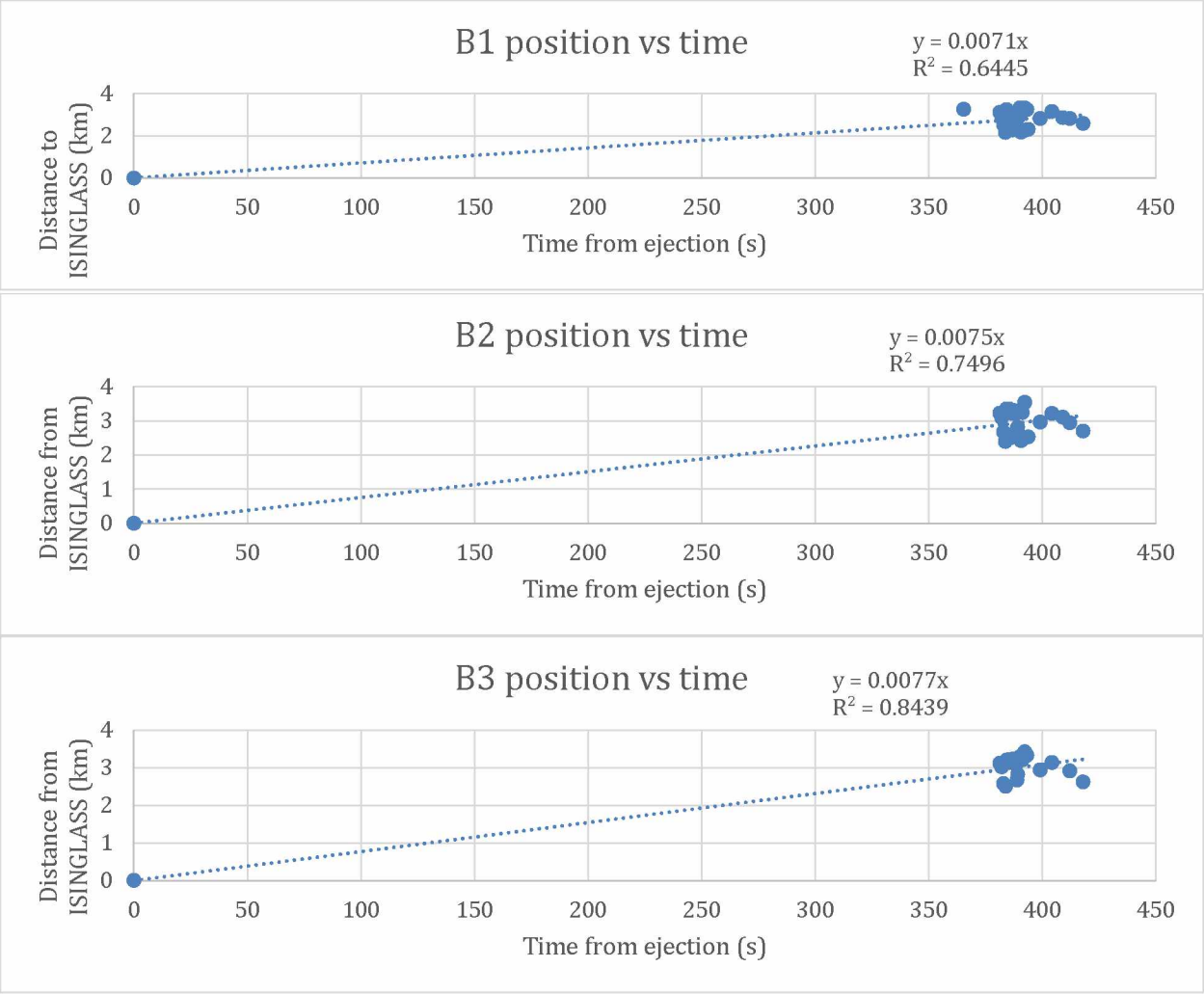

Figure 18: Resulting data sets showing position from main payload vs time from ejection. The resulting slope represents the relative velocity of the Bobs from the rocket, in (km/s). Data points are from the timing over which the beacons were turned on (~50 seconds), with a point initially at the time where the Bobs left the main payload.

In order to gain an understanding of the general behavior of each Bob, outputs of latitude, longitude, and altitude were used to convert into spatial dimensions, using equation 6 below. Uncertainties given by the skytracker program work in the same way, though uncertainty propagation will be discussed in section 5.3. The outputs used for Figure 18 were created through a GPS file for the main payload. On further analysis, the validity of the trajectory of the main came under question, so supplementary calculations were done comparing relative positions and velocities of each of the Bobs to one another. The results of these comparisons are shown in Figures

19-21, giving relative longitude (dx), latitude (dy), altitude (dz), and total speed (ds). Uncertainties in these measurements will also be discussed in section 5.3.

$$dx = Longitude\ Separation = |Long1 - Long2| * 111\frac{km}{deg} * \cos(Lat(avg) * \frac{\pi}{180})$$
$$dy = Latitude\ Separation = 111\frac{km}{degree} * |Lat1 - Lat2|$$
$$dz = Altitude\ Separation = |Alt1 - Alt2|$$
$$ds = Total\ Separation = \sqrt{dx^2 + dy^2 + dz^2}$$
$$Lat(avg) = \frac{1}{2}(Lat1 + Lat2) \quad (6)$$

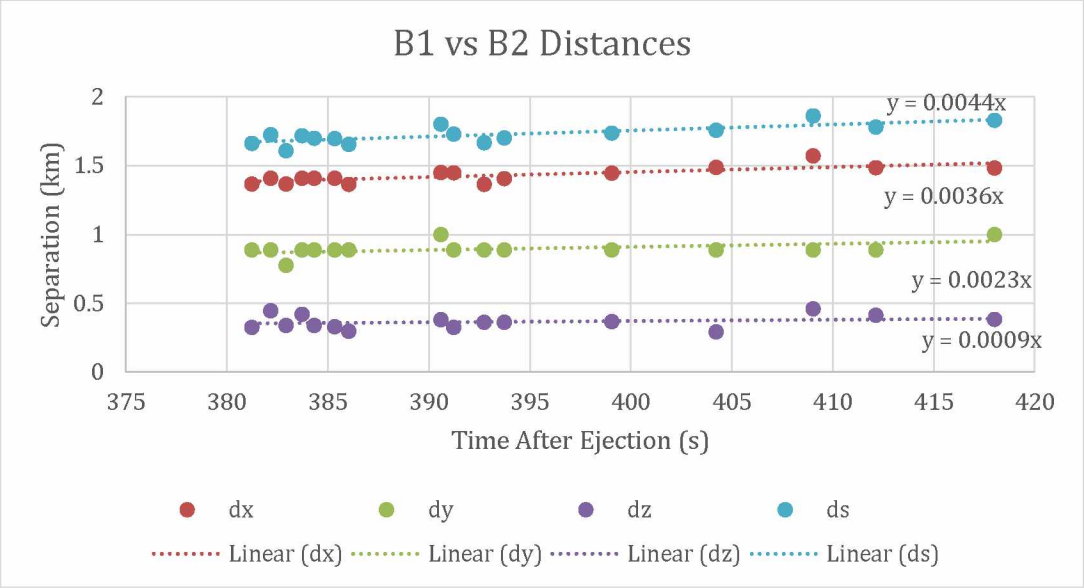

Figure 19: Plot comparing latitude, longitude, altitude, and total distance for Bobs B1 and B2. The slope of each line is the rate of change (velocity), with units of km/s.

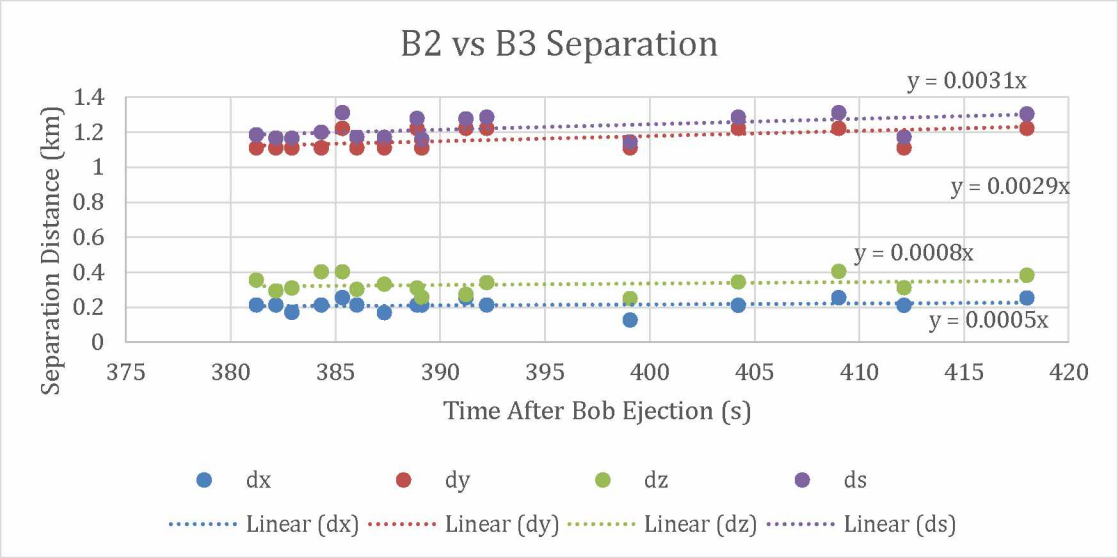

Figure 20: Plot comparing latitude, longitude, altitude, and total distance for Bobs B2 and B3. The slope of each line is the rate of change (velocity), with units of km/s.

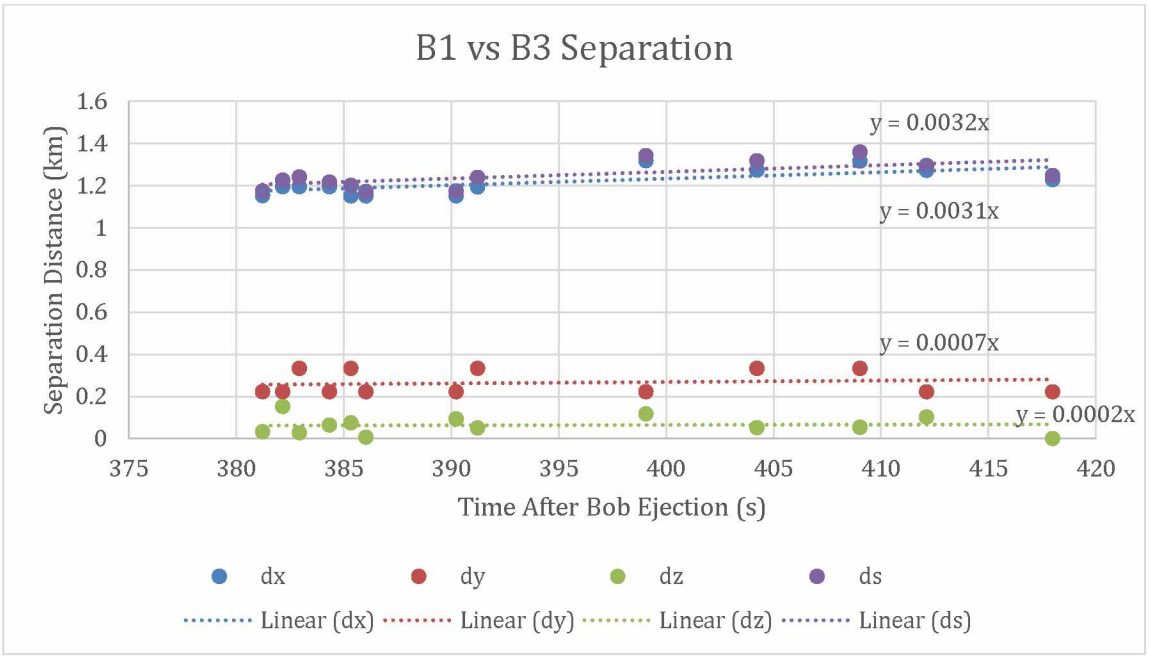

Figure 21: Plot comparing latitude, longitude, altitude, and total distance for Bobs B1 and B3. The slope of each line is the rate of change (velocity), with units of km/s.

The tables below summarize the findings from Figures 19-21. Uncertainty will be discussed in section 5.3, below. Values can be seen in Appendix III, and the relative latitude, longitude, and altitude of the Bobs between the main and each other are summarized below. For the purpose of showing speeds, magnitudes are shown.

Relative Latitude Speed	B2	B3
B1	2.3 m/s	0.7 m/s
B2	0 m/s	2.9 m/s
		0 m/s

Table 3: Relative Latitude Speeds ($\Delta x/\Delta t$) of the Bobs

Relative Longitude Speed	B2	B3
B1	3.6 m/s	3.1 m/s
B2	0 m/s	0.5 m/s
		0 m/s

Table 4: Relative Longitude Speeds ($\Delta y/\Delta t$) of the Bobs

Relative Altitude Speed	B2	B3
B1	0.9 m/s	0.2 m/s
B2	0 m/s	0.8 m/s
B3		0 m/s

Table 5: Relative Altitude Speeds ($\Delta z/\Delta t$) of the Bobs

Relative Speed	B1	B2	B3
Main	7.1 m/s	7.5 m/s	7.7 m/s
B1	0 m/s	4.4 m/s	3.2 m/s
B2		0 m/s	3.1 m/s
B3			0 m/s

Table 6: Relative Total Speed of the Bobs

5.3 Uncertainty Analysis

In order to determine spatial gradient scale importance from the magnetometer and PIP data, it was important to understand where in space these measurements occurred. After scientific data collection, the beacons were turned on in order to determine position and velocity components of the Bobs. From this triangulation, position of the Bobs during data collection could be calculated. For meaningful analysis, velocity and position calculations of the beacon triangulation must include uncertainty. Determination of the accuracy to which this data is known is important. While raw uncertainties can be found in data in Appendix III as outputs of the Skytracker program,

the propagation of uncertainty when performing relative uncertainties requires calculation. All events where the three photos were taken outside of .01s of each other were discarded, so that uncertainty in the timing could be neglected.

For uncertainties in the Latitude, Longitude, and Altitude, the uncertainties given by the Skytracker program were used. In order to find this uncertainty, the program uses a Monte Carlo algorithm with 256 distinct points. Using only possible points inside the error ellipse specified (see Figure 11), the program uses a least squares method to determine the maximum error. These values are given in degrees, so the conversion to km must be made (see equation 6 above).

Once these errors are calculated by the program, the output can be used to calculate error in relative position. By using the propagation of spatial error: $\sqrt{dx^2 + dy^2 + dz^2}$, the error in each position measurement can be calculated. By performing a standard deviation calculation, the error for the slope of this line, the velocity, can be calculated. Tables 7-10 below summarize the found uncertainties for the relative velocity of each bob with respect to the main as well as the relative uncertainties in latitude, longitude, and altitude. The method of calculating these uncertainties is shown through equation 7, and a full output of the distances, as well as uncertainties is found in Appendix V. In order to find the uncertainty in the speed calculation, an average uncertainty was taken for each component, and this average was divided by the total time. This can be done since the relative distances are all within ~40 seconds compared to the ~400 seconds since ejection. For the purpose of these calculations, t = 400 s was used.

$$ddx = Longitude\ Uncertainty = \sqrt{(dx.1)^2 + (dx.2)\text{^}2}$$

$$ddy = Latitude\ Uncertainty = \sqrt{(dy.1)^2 + (dy.2)\text{^}2}$$

$$ddz = Altitude\ Uncertainty = \sqrt{(dz.1)^2 + (dz.2)\text{^}2}$$

$$dds = Total\ Uncertainty = \sqrt{ddx^2 + ddy^2 + ddz\text{^}2}$$

$$\text{Speed Uncertainty} = \frac{dv}{dx} delx = \frac{1}{t} delx = \frac{\overline{dd\_}}{400} \quad (7)$$

Relative Latitude Speed Uncertainty	B2	B3
B1	0.529 m/s	0.552 m/s
B2	0 m/s	0.508 m/s
B3		0 m/s

Table 7: Relative Latitude Speed Uncertainty (+/- dx/dt)

Relative Longitude Speed Uncertainty	B2	B3
B1	0.349 m/s	0.355 m/s
B2	0 m/s	0.323 m/s
B3		0 m/s

Table 8: Relative Longitude Speed Uncertainty (+/- dy/dt)

Relative Altitude Speed Uncertainty	B2	B3
B1	0.953 m/s	0.989 m/s
B2	0 m/s	0.944 m/s
B3		0 m/s

Table 9: Relative Altitude Speed Uncertainty (+/- dz/dt)

Relative Speed Uncertainty	B1	B2	B3
Main	0.793 m/s	0.778 m/s	0.757 m/s
B1	0 m/s	1.160 m/s	1.201 m/s
B2		0 m/s	1.137 m/s
B3			0 m/s

Table 10: Relative Total Speed Uncertainty

It can be seen that these values are exceedingly high, with a relative uncertainty of ~30% being the highest, and therefore there is large uncertainty in the determinations, however it is important to know relative velocities and positions from multiple sources to get a general understanding of the behavior of these objects and to make sense of the incoming data.

5.4 Implications for ISINGLASS and future missions

The main research goal of ISINGLASS is to determine the spatial gradient scale length, dN/dx, over which electric field, magnetic field, and ion population parameters (such as density change and induced charge) matter in models of ionosphere-magnetosphere coupling. Specifically important is the ability to measure the scale lengths of auroral arcs in the upper ionosphere. These bulk parameters are present in every model and difference between fine and course simulation leads to differing outcomes. For this reason, determination of the spatial gradient scale lengths is important to the accuracy of such models. Determinations of multiple scale lengths are possible over the course of each launch due to positioning of instruments, so data from each launch can be used. Scale lengths seen are that of the rocket (~30 m), the spread of the Bobs (~6 km), and over the arc of the rocket flight (~250 km). While the Bobs did not eject in the first launch, most instruments were still functioning on board the main, so differences in readings across the rocket and the flight path can be calculated. The second launch was successful, so comparison across all three spatial length scales can be made.

In order to make these calculations, it is important to take measurements of bulk parameters, such as thermal ion population and magnetic field, and vitally important to understand where in space these measurements occur. Measurements of thermal ion population and magnetic field are important aspects seen through analysis of instruments on board. The spatial determinations over which this data takes place was my responsibility. Determining dx of the dN/dx was accomplished through trajectory analysis of the Bobs. While each Bob contained an accelerometer, due to the uncertainty of these devices it was essential to take optical data and analyze the position data through an alternative method. The method of calculating positions through optical data served both as calibration of the accelerometer and confirmation of the data obtained.

While analysis of the data is ongoing, certain determinations have already been made. With experimental rocketry, it is often difficult to know if changes in measurements are due to bulk changes in what is being measured, or are being changed due to influence of the rocket on local plasma conditions. By targeting a wider range of spatial scale, these bulk changes can be better understood, and noise from instruments onboard the rocket can be reduced. So far it has been found

that, while there is some noise from the rocket and Bobs passing through, differences can be seen between instruments, showing the existence of a critical spatial scale. This means that there exists a clear need to do further experimentation in order to fine-tune this determination of spatial scale.

Even though the work will be done by the Principal Investigator, a sample pathway to closure is as follows. Using the relative velocity data generated here, relative positions of each of the Bobs can be calculated over the course of ejection to the beacons turning on. This will give distances between the Bobs at specified times. When paired with the data from instruments on board the Bobs, scale lengths can be determined by the relative distances of the Bobs with each other when differences in measurements are detected. It is important to pair this data with ground based instruments in order to eliminate already present ionospheric gradients. Issues arising with external gradients and fronts are eliminated by having 4 Bobs ejected, and auroral movement and interference can be seen through delayed readings when all data is interpolated.

A secondary goal of the ISINGLASS mission is to test a novel approach to measurements of such data. Unique to this project is the use, in tandem, of data from ejected Bobs as well as the many instruments on board the main and the Bobs: APES, ERPA, PIPs, and COWBOY. Additionally, the software used for determination of position through optical data was novel for this application. Ultimately, the successes of ISINGLASS present a pathway through further analysis and a future mission in order to determine the spatial gradient scale length necessary for models of the upper ionosphere.

Chapter 6: Conclusion

For a Master's Project in Physics, I spent a month at Toolik Field Station on the North Slope of Alaska serving as an optical collector for ISINGLASS: a NASA campaign hoping to determine spatial scale lengths in order to strengthen preexisting models of magnetosphere-ionosphere interactions. Not only did this experiment test the accuracy of preexisting models, but also tested a novel method for mapping the position of small rocket sub-payloads in Alaska using optical observation sites, strong LED beacons, and a software designed for TMA release. This is vital for further research and determining the parameters for which this method can be used in future missions.

While at Toolik, I also performed tasks relevant to the mission, implementing and troubleshooting a new piece of hardware on a Scanning Doppler Imager as well as installing and calibrating a Spectrometer. After data collection, I analyzed the images from all relevant field sites in order to find position and trajectories of magnetometer/thermal gradient Bobs, which when paired with the data from their onboard magnetometer and Petite Ion Probe would help to answer the PI's research question.

Through this study, it was determined that the method used was valid across the distance spread in this experiment, ~400 km between optical sites, managing to quantify the positions of the rocket sub-payloads to a strong degree of accuracy using three optical sites. While the data from instruments on board the main and sub-payloads is still being processed, the instruments registered both magnetometer and thermal ion density data which, when interpreted with the position data, should give useful information for determining scale lengths.

There have been many successes in my part of the mission. At this point, we know the position of the Bobs, as well as accurate timings of when they were ejected. While the data has an issue with determining the velocities, from the straightforward distance/time calculation I have approximated the velocities, which can be used to filter out noise from the PIP and magnetometer data. We learned that on the second flight the Bobs left the main payload, and now have a baseline from which future experiments can be designed using this method of data collection, which we have determined is feasible and reliable. We learned how accurately we can determine the position

of the Bobs, and most importantly, that we can see the beacons from hundreds of kilometers away, in spite of the intensity constraints of the LED beacons ($1/r^2$).

While there are still questions about the determination of the spatial scale for which the Zettergren model is most accurate, we now have all the data we need in order to determine these parameters once the PIP data and magnetometer data has been processed. This is taking longer due to uncertainty in the processing and assessing of the assumptions within the sheath. My role was to calculate the positions and acquire data, and give the PI the data she needs in order to answer the research question. We will learn about the plasma physics when the data is combined with the created baselines.

Appendix I: Timeline of Isinglass Launches

Time	Event	Nom. Alt. (km)	Nominal Range (km)
0 min. 0 sec.	Terrier Ignition	0.2	0.0
0 min. 0.5 sec.	Rail Release	0.2	0.0
0 min. 0.9 sec.	spin motor ignition	0.2	0.0
0 min. 1 sec.	Main Payload WASP set/reset	0.2	0.0
0 min. 1 sec.	Sub-Payload WASP set/reset	0.2	0.0
0 min. 6.2 sec.	Terrier Burnout	2.1	0.3
0 min. 12 sec.	BB Ignition	5.1	0.8
0 min. 46 sec.	BB Burnout	48.6	10.7
1 min. 2 sec.	Motor Separation	85.2	19.9
1 min. 3 sec.	ACS1 trim roll/rate damping	87.4	20.5
1 min. 10 sec.	ACS1 complete	102.6	24.5
1 min. 11 sec.	Sub-payload Skirt Separation	104.7	25.1
1 min. 12 sec.	NC Separation	106.8	25.6
1 min. 13 sec.	ACS2 align to -B	108.9	26.2
1 min. 27 sec.	ACS2 complete	137.5	34.1
1 min. 28 sec.	Sub-payload Separation	139.4	34.7
1 min. 30 sec.	Aft Skirt Separation	143.3	35.8
1 min. 31 sec.	ACS3 trim roll, align to BOB target	145.3	36.3
1 min. 38 sec.	Sub-payload Power Amp ON/OFF	158.6	40.3
1 min. 41 sec.	Sub-payload Deploy Booms	164.2	41.9
2 min. 1 sec.	BOB doors deploy	199.2	53.0
2 min. 2 sec.	BOBs deploy	200.8	53.6
2 min. 4 sec.	ACS3 complete	204.1	54.7
2 min. 4 sec.	ACS4 trim roll and align to -B	204.1	54.7
2 min. 24 sec.	ACS4 complete	234.9	65.7
2 min. 24 sec.	APES HV ON	234.9	65.7
2 min. 33 sec.	Sub-payload Engage Brake	247.6	70.6
5 min. 7.1 sec.	Apogee (nominal)	352.3	152.6
8 min. 21 sec.	BOB 45 & 315 beacon ON	186.1	256.5
8 min. 22 sec.	BOB 135 & 225 beacon ON	184.3	257.1
9 min. 10.1 sec.	90 km Down-leg (nominal)	89.9	284.2
9 min. 34 sec.	APES HV OFF	35.3	297.8
9 min. 34 sec.	ACS vent	35.3	297.8
10 min. 21 sec.	Ballistic Impact (nominal)	0.0	305.3

Appendix II: Sample Output from Trajectory File

What follows is a sample output from the Skytracker program written by Mark Conde. Because the full output file is 74 pages, I have chosen only to include two instances of target B1, the first bob. It can be seen that the output file contains temporal data, latitude, longitude, and altitude data with uncertainty, images used, and distance from the main payload.

Skytracker Batch Process ASCII Export for Data in Project File: C:\triangulation\ISINGLASS_2017\triangulation\conde_3_ISINGLASS_2107_new_triangulation_16_Aug_2017.IDL_save

```
=== Begin Header
   Export Time: 2018-Feb-17 at 03:28:56
   Project Name: ISINGLASS_2017
   Principal Investigator: Lynch
   Locale: Poker
   Agency: NASA
   Analyst: Conde
=== End Header

>>> Begin Triangulation: B1
*** Begin  Summary: B1
   Target Name: B1
   Mean Observation Time: 2017-Mar-02 at 07:58:46.332 UT
   Lon: -146.721 deg +/- 0.003 deg
   Lat: 67.488 deg +/- 0.002 deg
   Alt: 165.165 km +/- 246.017 meters
   Number of Contributing Images: 3
   Distance from Trajectory Object ISINGLASS_2017 at 07:58:46.332 UT to target B1 was 3.164 km
*** End Summary: B1
### Begin Details: B1
--- Begin Contributing Observation Description: B1
            Image File: cld-new\cldnoframes\IGLASS_CLD_20170302_075846_333.tif
                 Site:  Coldfoot
               Camera: A7
       Observation Time: 2017-Mar-02 at 07:58:46.332 UT
         Target Azimuth: 78.289 deg +/- 0.050 deg
       Target Elevation: 46.744 deg +/- 0.050 deg
           Slant Range: 224.643 km
         Miss Distance: 0.126 km
  Monte-Carlo Iterations: 256
     Triangulation Time: 2018-Feb-17 at 03:28:39 UT
               Analyst: Conde
--- End Contributing Observation Description: B1
--- Begin Contributing Observation Description: B1
            Image File: vee-new\veenoframes\IGLASS_VEE_20170302_075846_333.tif
                 Site:  Venetie
               Camera: A7
       Observation Time: 2017-Mar-02 at 07:58:46.332 UT
         Target Azimuth: -14.221 deg +/- 0.054 deg
       Target Elevation: 71.330 deg +/- 0.176 deg
           Slant Range: 174.013 km
         Miss Distance: 0.069 km
  Monte-Carlo Iterations: 256
```

Triangulation Time: 2018-Feb-17 at 03:28:39 UT
Analyst: Conde
--- End Contributing Observation Description: B1
--- Begin Contributing Observation Description: B1
Image File: pkr-new\pkrnoframes\PKR_CANON_20170302_075846_333.BMP
Site: Poker
Camera: EM20
Observation Time: 2017-Mar-02 at 07:58:46.332 UT
Target Azimuth: 6.581 deg +/- 0.050 deg
Target Elevation: 30.417 deg +/- 0.050 deg
Slant Range: 316.159 km
Miss Distance: 0.142 km
Monte-Carlo Iterations: 256
Triangulation Time: 2018-Feb-17 at 03:28:39 UT
Analyst: Conde
--- End Contributing Observation Description: B1
End Details: B1
>>> End Triangulation: B1

>>> Begin Triangulation: B1
*** Begin Summary: B1
Target Name: B1
Mean Observation Time: 2017-Mar-02 at 07:58:51.130 UT
Lon: -146.710 deg +/- 0.003 deg
Lat: 67.511 deg +/- 0.002 deg
Alt: 155.893 km +/- 230.270 meters
Number of Contributing Images: 3
Distance from Trajectory Object ISINGLASS_2017 at 07:58:51.130 UT to target B1 was 2.863 km
*** End Summary: B1
Begin Details: B1
--- Begin Contributing Observation Description: B1
Image File: cld-new\cldnoframes\IGLASS_CLD_20170302_075851_132.tif
Site: Coldfoot
Camera: A7
Observation Time: 2017-Mar-02 at 07:58:51.133 UT
Target Azimuth: 77.329 deg +/- 0.050 deg
Target Elevation: 44.933 deg +/- 0.050 deg
Slant Range: 218.487 km
Miss Distance: 0.121 km
Monte-Carlo Iterations: 256
Triangulation Time: 2018-Feb-17 at 03:28:39 UT
Analyst: Conde
--- End Contributing Observation Description: B1
--- Begin Contributing Observation Description: B1
Image File: vee-new\veenoframes\IGLASS_VEE_20170302_075851_132.tif
Site: Venetie
Camera: A7
Observation Time: 2017-Mar-02 at 07:58:51.133 UT
Target Azimuth: -13.096 deg +/- 0.046 deg
Target Elevation: 69.538 deg +/- 0.164 deg
Slant Range: 166.067 km
Miss Distance: 0.107 km
Monte-Carlo Iterations: 256
Triangulation Time: 2018-Feb-17 at 03:28:39 UT
Analyst: Conde
--- End Contributing Observation Description: B1

--- Begin Contributing Observation Description: B1
Image File: pkr-new\pkrnoframes\PKR_CANON_20170302_075851_125.BMP
Site: Poker
Camera: EM20
Observation Time: 2017-Mar-02 at 07:58:51.125 UT
Target Azimuth: 6.612 deg +/- 0.050 deg
Target Elevation: 28.720 deg +/- 0.050 deg
Slant Range: 313.571 km
Miss Distance: 0.142 km
Monte-Carlo Iterations: 256
Triangulation Time: 2018-Feb-17 at 03:28:39 UT
Analyst: Conde
--- End Contributing Observation Description: B1
End Details: B1
>>> End Triangulation: B1

Appendix III: Data output from Skytracker, showing degree coordinates and uncertainties. Output converted into km is given in appendix IV. One important note is that the Time is not absolute time, and each refers to UT 07:58:XX.XXX. When calculations were made, a shift of -357.9 s was applied, making the metric time from release.

B1							
Time (s)	Longitude (deg)	Longitude uncertainty (deg)	Latitude (deg)	Latitude uncertainty (deg)	Altitude (km)	altitude uncertainty (m)	Distance (km)
23.332	-146.774	0.002	67.378	0.001	206.254	232.357	3.111
24.266	-146.771	0.002	67.382	0.001	204.831	305.018	2.869
25.033	-146.769	0.005	67.385	0.002	203.45	477.91	2.521
25.832	-146.767	0.002	67.389	0.001	202.142	254.594	2.158
26	-146.767	0.002	67.39	0.001	201.857	221.147	2.438
26.434	-146.766	0.002	67.392	0.001	201.053	243.127	3.25
27.434	-146.764	0.002	67.397	0.001	199.328	265.871	3.257
28.131	-146.769	0.002	67.401	0.001	197.765	332.089	3.011
30.232	-146.758	0.002	67.41	0.001	194.524	246.871	2.87
32.332	-146.756	0.002	67.421	0.001	190.52	263.91	3.329
32.792	-146.753	0.001	67.423	0.001	189.924	164.755	2.179
33.833	-146.75	0.002	67.428	0.001	188.123	170.341	2.238
34.832	-146.75	0.002	67.433	0.001	186.235	218.598	2.281
35.832	-146.747	0.001	67.437	0.001	184.426	130.665	2.306
41.167	-146.733	0.003	67.463	0.003	174.844	336.546	2.818
46.332	-146.721	0.003	67.488	0.002	165.165	246.017	3.164
51.13	-146.71	0.003	67.511	0.002	155.893	230.27	2.863
54.232	-146.703	0.002	67.527	0.001	150.139	276.057	2.814
60.1	-146.69	0.003	67.556	0.002	138.41	323.751	2.586
B2							
Time (s)	Longitude (deg)	Longitude uncertainty (deg)	Latitude (deg)	Latitude uncertainty (deg)	Altitude (km)	altitude uncertainty (m)	Distance (km)
23.332	-146.806	0.002	67.37	0.001	205.93	299.894	3.228
24.266	-146.804	0.002	67.374	0.001	204.384	268.903	3.089
25.033	-146.801	0.002	67.378	0.001	203.112	308.476	2.675
25.832	-146.8	0.002	67.381	0.001	201.721	244.993	2.393
26.434	-146.799	0.002	67.384	0.001	200.715	338.461	3.356
27.434	-146.797	0.002	67.389	0.001	198.999	298.11	3.358
28.131	-146.801	0.002	67.393	0.001	197.469	360.923	3.225
28.965	-146.794	0.002	67.396	0.001	196.409	332.404	2.525
29.434	-146.792	0.002	67.399	0.001	195.601	330.314	3.304
30.238	-146.793	0.001	67.402	0.001	193.994	203.577	3.197

30.999	-146.79	0.002	67.406	0.001	192.668	188.936	2.779
31.224	-146.786	0.001	67.408	0.001	192.586	161.399	2.815
32.702	-146.787	0.002	67.414	0.001	189.543	188.023	2.427
33.332	-146.785	0.001	67.417	0.001	188.654	168.788	3.249
34.332	-146.784	0.002	67.422	0.001	186.593	167.984	3.541
34.832	-146.782	0.002	67.425	0.001	185.872	253.254	2.515
35.832	-146.78	0.001	67.429	0.001	184.064	158.969	2.528
41.167	-146.767	0.003	67.455	0.003	174.476	238.1	2.967
46.332	-146.756	0.003	67.48	0.002	164.872	265.009	3.221
51.13	-146.747	0.003	67.503	0.002	155.434	294.921	3.108
54.232	-146.738	0.003	67.519	0.001	149.725	289.234	2.951
60.1	-146.725	0.004	67.547	0.002	138.028	344.59	2.705
B3							
Time (s)	Longitude (deg)	Longitude uncertainty (deg)	Latitude (deg)	Latitude uncertainty (deg)	Altitude (km)	altitude uncertainty (m)	Distance (km)
23.332	-146.801	0.002	67.38	0.001	206.286	280.236	3.117
24.266	-146.799	0.002	67.384	0.001	204.678	337.75	3.02
25.033	-146.797	0.002	67.388	0.001	203.422	248.554	2.572
26	-146.795	0.002	67.393	0.001	201.805	297.678	2.501
26.434	-146.794	0.002	67.394	0.001	201.118	276.349	3.199
27.434	-146.791	0.002	67.4	0.001	199.403	320.038	3.212
28.131	-146.796	0.002	67.403	0.001	197.772	322.415	3.122
29.434	-146.788	0.002	67.409	0.001	195.934	376.743	3.227
30.238	-146.788	0.002	67.413	0.001	194.295	217.453	3.112
30.999	-146.785	0.002	67.417	0.001	192.979	212.813	2.663
31.224	-146.781	0.001	67.418	0.001	192.844	179.696	2.813
32.332	-146.783	0.001	67.423	0.001	190.613	177.725	3.289
33.332	-146.779	0.001	67.428	0.001	188.928	174.585	3.203
34.332	-146.779	0.001	67.433	0.001	186.934	156.232	3.421
35.332	-146.776	0.002	67.438	0.001	185.259	199.952	3.32
41.167	-146.764	0.002	67.465	0.002	174.726	197.754	2.939
46.332	-146.751	0.003	67.491	0.002	165.217	261.097	3.133
51.13	-146.741	0.003	67.514	0.002	155.84	279.297	2.924
54.232	-146.733	0.003	67.529	0.002	150.037	317.099	2.914
60.1	-146.719	0.002	67.558	0.001	138.411	258.149	2.613

Appendix IV: Skytracker longitude, latitude, altitude, and total distance and uncertainty output in km. It is important to note that while Latitude and Longitude are given here in absolute km readings, these are only used for relative comparisons. Timings are the same as above, but omitted due to spatial constraints.

B1						
Latitude (km)	Latitude uncertainty (km)	Longitude (km)	Longitude uncertainty (km)	Altitude (km)	Altitude uncertainty (km)	Uncertainty (km)
7478.958	0.111	-6266.68116	0.085392252	206.254	0.232357	0.271298013
7479.402	0.111	-6265.5032	0.085377945	204.831	0.305018	0.335628327
7479.735	0.222	-6264.6304	0.213418038	203.45	0.47791	0.568532521
7480.179	0.111	-6263.49513	0.085352908	202.142	0.254594	0.290558469
7480.29	0.111	-6263.23265	0.085349331	201.857	0.221147	0.261747023
7480.512	0.111	-6262.66502	0.085342178	201.053	0.243127	0.280561981
7481.067	0.111	-6261.26725	0.085324293	199.328	0.265871	0.300480654
7481.511	0.111	-6260.43056	0.085309985	197.765	0.332089	0.360391311
7482.51	0.111	-6257.5989	0.085277789	194.524	0.246871	0.28379322
7483.731	0.111	-6254.62602	0.085238437	190.52	0.26391	0.298722412
7483.953	0.111	-6253.97313	0.042615641	189.924	0.164755	0.203178008
7484.508	0.111	-6252.53269	0.085213393	188.123	0.170341	0.220450399
7485.063	0.111	-6251.22005	0.085195503	186.235	0.218598	0.259546449
7485.507	0.111	-6250.04213	0.042590596	184.426	0.130665	0.176658714
7488.393	0.333	-6242.61997	0.127632229	174.844	0.336546	0.490349055
7491.168	0.222	-6235.5454	0.127498015	165.165	0.246017	0.355055077
7493.721	0.222	-6229.0384	0.127374516	155.893	0.23027	0.34428555
7495.497	0.111	-6224.5394	0.084859061	150.139	0.276057	0.309401887
7498.716	0.222	-6216.37151	0.127132828	138.41	0.323751	0.412627515
B2						
Latitude (km)	Latitude uncertainty (km)	Longitude (km)	Longitude uncertainty (km)	Altitude (km)	Altitude uncertainty (km)	Uncertainty (km)
7478.07	0.111	-6270.1476	0.085420863	205.93	0.299894	0.33098963
7478.514	0.111	-6269.01213	0.085406557	204.384	0.268903	0.30318988
7478.958	0.111	-6267.83396	0.085392252	203.112	0.308476	0.338777625
7479.291	0.111	-6267.0037	0.085381522	201.721	0.244993	0.282192442
7479.624	0.111	-6266.17344	0.085370792	200.715	0.338461	0.366285436
7480.179	0.111	-6264.77543	0.085352908	198.999	0.29811	0.32935648
7480.623	0.111	-6263.89596	0.085338601	197.469	0.360923	0.387129292
7480.956	0.111	-6262.80966	0.08532787	196.409	0.332404	0.360685825
7481.289	0.111	-6261.93671	0.085317139	195.601	0.330314	0.35875807
7481.622	0.111	-6261.19173	0.042653204	193.994	0.203577	0.235762361

7482.066	0.111	-6260.01357	0.085292099	192.668	0.188936	0.235143688
7482.288	0.111	-6259.3179	0.042642472	192.586	0.161399	0.200471987
7482.954	0.111	-6257.7852	0.08526348	189.543	0.188023	0.234400319
7483.287	0.111	-6256.91225	0.042626374	188.654	0.168788	0.206464032
7483.842	0.111	-6255.55678	0.085234859	186.593	0.167984	0.218642643
7484.175	0.111	-6254.68383	0.085224126	185.872	0.253254	0.289347093
7484.619	0.111	-6253.54831	0.042604907	184.064	0.158969	0.198512773
7487.505	0.333	-6246.16737	0.127675173	174.476	0.2381	0.428814132
7490.28	0.222	-6239.134	0.127540966	164.872	0.265009	0.368484013
7492.833	0.222	-6232.71069	0.127417474	155.434	0.294921	0.390509422
7494.609	0.111	-6228.12589	0.127331555	149.725	0.289234	0.3349487
7497.717	0.222	-6220.21915	0.169574896	138.028	0.34459	0.443601075
B3						
Latitude (km)	Latitude uncertainty (km)	Longitude (km)	Longitude uncertainty (km)	Altitude (km)	Altitude uncertainty (km)	Uncertainty (km)
7479.18	0.111	-6267.30892	0.085385098	206.286	0.280236	0.313279158
7479.624	0.111	-6266.17344	0.085370792	204.678	0.33775	0.365628547
7480.068	0.111	-6265.03796	0.085356485	203.422	0.248554	0.285282002
7480.623	0.111	-6263.63994	0.085338601	201.805	0.297678	0.328961804
7480.734	0.111	-6263.33474	0.085335024	201.118	0.276349	0.309793215
7481.4	0.111	-6261.63151	0.085313562	199.403	0.320038	0.349318945
7481.733	0.111	-6261.05713	0.08530283	197.772	0.322415	0.351495384
7482.399	0.111	-6259.14063	0.085281367	195.934	0.376743	0.401906954
7482.843	0.111	-6258.09039	0.085267057	194.295	0.217453	0.258606416
7483.287	0.111	-6256.91225	0.085252747	192.979	0.212813	0.254712394
7483.398	0.111	-6256.47918	0.042624585	192.844	0.179696	0.215472754
7483.953	0.111	-6255.2516	0.042615641	190.613	0.177725	0.213829999
7484.508	0.111	-6253.76828	0.042606696	188.928	0.174585	0.211225597
7485.063	0.111	-6252.45538	0.042597752	186.934	0.156232	0.196326275
7485.618	0.111	-6251.01467	0.085177613	185.259	0.199952	0.244043087
7488.615	0.222	-6243.4136	0.085080995	174.726	0.197754	0.309240069
7491.501	0.222	-6236.03246	0.127481907	165.217	0.261097	0.365660061
7494.054	0.222	-6229.5666	0.127358406	155.84	0.279297	0.378828428
7495.719	0.222	-6225.28692	0.12727785	150.037	0.317099	0.407474449
7498.938	0.111	-6217.07504	0.084748056	138.411	0.258149	0.293503218

Appendix V: Position, Uncertainty, and Velocity Separation Data between Bobs

B1 vs. B2 Separation Data

dx	dy	dz	ds	Lat Unc	Long Unc	Alt unc	Total unc	Time
1.366508	0.888	0.324	1.661585	0.156978	0.120763	0.379376	0.427963	358.328
1.408976	0.888	0.447	1.724403	0.156978	0.120743	0.406626	0.452289	358.3523
1.366079	0.777	0.338	1.607528	0.248204	0.229859	0.568819	0.661812	358.5618
1.408562	0.888	0.421	1.717508	0.156978	0.120708	0.353327	0.405033	358.305
1.408385	0.888	0.338	1.698922	0.156978	0.120692	0.416733	0.461384	358.3614
1.40809	0.888	0.329	1.69691	0.156978	0.120667	0.399446	0.445825	358.3458
1.365192	0.888	0.296	1.655267	0.156978	0.120647	0.490457	0.52891	358.4289
1.449209	0.999	0.381	1.800935	0.156978	0.095292	0.249994	0.310192	358.2102
1.449057	0.888	0.324	1.730112	0.156978	0.095284	0.271796	0.328016	358.228
1.36336	0.888	0.363	1.667053	0.156978	0.120485	0.334548	0.388692	358.2887
1.405729	0.888	0.362	1.701665	0.156978	0.060232	0.205778	0.265734	358.1657
1.446745	0.888	0.368	1.736963	0.470933	0.1805	0.412256	0.651393	358.5514
1.487731	0.888	0.293	1.757196	0.313955	0.18031	0.361599	0.511697	358.4117
1.571221	0.888	0.459	1.862246	0.313955	0.180135	0.374169	0.520595	358.4206
1.485288	0.888	0.414	1.779331	0.156978	0.152982	0.39983	0.455971	358.356
1.483502	0.999	0.382	1.828853	0.313955	0.211889	0.472818	0.605823	358.5058
		Average	Uncertainty:	0.211735	0.139449	0.381098	0.463833	
		Velocity	Uncertainty:	0.529337	0.348623	0.952746	1.159583	

B2 vs. B3 Separation Data

dx	dy	dz	ds	Lat Unc	Long Unc	Alt unc	Total unc	Time
0.213508	1.11	0.356	1.185083	0.156978	0.120804	0.410449	0.455746	358.3557
0.213472	1.11	0.294	1.16795	0.156978	0.120783	0.431722	0.474989	358.375
0.170749	1.11	0.31	1.165056	0.156978	0.120763	0.396152	0.442902	358.3429
0.213383	1.11	0.403	1.200017	0.156978	0.120733	0.436949	0.479732	358.3797
0.256	1.221	0.404	1.311333	0.156978	0.120708	0.437372	0.480111	358.3801
0.213302	1.11	0.303	1.170217	0.156978	0.120687	0.48396	0.5229	358.4229
0.170599	1.11	0.333	1.171364	0.156978	0.120657	0.501042	0.538742	358.4387
0.213182	1.221	0.311	1.277892	0.156978	0.120622	0.284581	0.346667	358.2467
0.213168	1.11	0.258	1.159355	0.156978	0.060306	0.241537	0.294311	358.1943
0.2557	1.221	0.274	1.277223	0.156978	0.060283	0.242836	0.295373	358.1954
0.213038	1.221	0.341	1.285499	0.156978	0.095296	0.229406	0.293854	358.1939
0.127649	1.11	0.25	1.144943	0.400216	0.153447	0.309513	0.528694	358.4287
0.21252	1.221	0.345	1.28648	0.313955	0.180371	0.372023	0.519137	358.4191
0.254776	1.221	0.406	1.311712	0.313955	0.180196	0.406184	0.544081	358.4441
0.212175	1.11	0.312	1.172375	0.248204	0.180074	0.429195	0.527484	358.4275
0.254304	1.221	0.383	1.304684	0.248204	0.189591	0.430561	0.531914	358.4319
		Average	Uncertainty:	0.203206	0.129082	0.377718	0.45479	
		Velocity	Uncertainty:	0.508014	0.322706	0.944294	1.136974	

B1 vs. B3 Separation Data

dx	dy	dz	ds	Lat Unc	Long Unc	Alt unc	Total unc	Time
1.15275	0.222	0.032	1.174368	0.156978	0.120763	0.364036	0.414425	358.3144
1.195244	0.222	0.153	1.225276	0.156978	0.120743	0.455095	0.496318	358.3963
1.195069	0.333	0.028	1.240912	0.248204	0.229859	0.538681	0.636095	358.5361
1.194743	0.222	0.065	1.216931	0.156978	0.120692	0.368075	0.417957	358.318
1.151808	0.333	0.075	1.201323	0.156978	0.120667	0.416067	0.460776	358.3608
1.151639	0.222	0.007	1.172862	0.156978	0.120647	0.462855	0.50342	358.4034
1.150673	0.222	0.093	1.175577	0.156978	0.0953	0.318174	0.367367	358.2674
1.193065	0.333	0.05	1.239675	0.156978	0.095284	0.275434	0.331036	358.231
1.318814	0.222	0.118	1.342564	0.400216	0.153395	0.390346	0.579718	358.4797
1.274903	0.333	0.052	1.3187	0.313955	0.18031	0.358742	0.509682	358.4097
1.316123	0.333	0.053	1.358631	0.313955	0.180135	0.361982	0.511906	358.4119
1.272835	0.222	0.102	1.29607	0.248204	0.152982	0.420427	0.511632	358.4116
1.228902	0.222	0.001	1.248793	0.248204	0.152795	0.414072	0.506366	358.4064
		Average	Uncertainty:	0.220891	0.141813	0.395691	0.480515	
		Velocity	Uncertainty:	0.552227	0.354533	0.989228	1.201288	

References

Akasofu, S. I. (1964), The Development of the Auroral Substorm, *Planetary Space Sci.,* **12,** 273.

Banks, P.M. & G. Kockarts, *Aeronomy*, Academic Press, New York, 1973.

Bougher, S. W., Pawlowski, D., Bell, J. M., Nelli, S., McDunn, T., Murphy, J. R., ... & Ridley, A. (2015). Mars Global Ionosphere-Thermosphere Model: Solar cycle, seasonal, and diurnal variations of the Mars upper atmosphere. *Journal of Geophysical Research: Planets*, *120*(2), 311-342.

Brekke, A. (1997), *Physics of the Upper Polar Atmosphere,* Wiley-Praxis Series in Atmospheric Physics, Wiley and Sons.

Cohen, I. J., M. R. Lessard, S. R. Kaeppler, S. R. B. and C. A. Kletzing, and A. V. Streltsov et al. (2013), Auroral current and electrodynamics structure (ACES) observations of ionospheric feedback in the Alfvén resonator and model responses, *JGR*, 118, doi: 10.1002/jgra.50348.

Conde, M., and R. W. Smith (1998), Spatial Structure in the thermospheric horizontal wind above Poker Flat, Alaska, during solar minimum, *J. Geophys. Res., 103,* doi: 10.1029/97JA03331

Connor, H. K., Zesta, E., Fedrizzi, M., Shi, Y., Raeder, J., Codrescu, M. V., & Fuller-Rowell, T. J. (2016). Modeling the ionosphere-thermosphere response to a geomagnetic storm using physics-based magnetospheric energy input: OpenGGCM-CTIM results. *Journal of Space Weather and Space Climate*, *6*, A25.

De Boer, J. D., J. A. Noel, and J. St-Maurice (2010), The effects of mesoscale regions of precipitation on the ionospheric dynamics, electrodynamics and electron density in the presence of strong ambient electric fields, *Ann. Geophys., 28*, doi: 10.5194/angeo-28-1345-2010.

Gelinas, L. J., K. A. Lynch, M. Kelley, and R. Collins, et al. (2005), Mesospheric charged dust layer: implications for neutral chemistry, *J. Geophys. Res., 110*, doi:10.1029/2004JA010,503.

Guillemant, S., V. Genot, J. M. Velez, R. Ergun, and P. Louarn (2012), Solar wind plasma interaction with Solar Probe Plus spacecraft, *Ann. Geo., 30*, 1075.

Guillemant, S., V. Genot, J. M. Velez, P. Sarrailh, A. Hilgers, and P. Louarn (2013), A simulation study of spacecraft electrostatic sheath changes with the heliocentric distances from 0.044 to 1 AU, *IEEE Transactions on Plasma Science PP, 99*, doi:10.1109/TPS.2013.2246193.

Hui, C. H., & Seyler, C. E. (1992). Electron acceleration by Alfvén waves in the magnetosphere. *Journal of Geophysical Research: Space Physics*, *97*(A4), 3953-3963.

Hull et al., A. J. (2010), Time development of field-aligned currents, potential drops, and plasma associated with an auroral poleward boundary intensification, *J. Geophys. Res., 115,* doi:10.1029/2009JA014751.

Johnson, J. R., & Cheng, C. Z. (1997). Kinetic Alfvén waves and plasma transport at the magnetopause. *Geophysical research letters*, *24*(11), 1423-1426.

Kelley, M. C. (1989), *The Earth's Ionosphere,* Academic Press.

Klatt et al., E. (2005), Sierra observations of Alfvénic processes in the topside auroral ionosphere, *J. Geophys Res., 110,* doi:10.1029/2004JA010,883.

Knudsen, D. J., M. C. Kelley, G. D. Earle, J. P. Vickrey, and M. H. Boehm (1990), Distinguishing Alfvén waves from quasi-static field structures associated with the discrete aurora: sounding rocket and hilat satellite measurements, *Geophys. Res. Lett., 17*, 921.

Lillensten, J., and P. Blelly (2002), The TEC and F2 parameters as tracers of the ionosphere and thermosphere, *J. Atmos. Solar Terr. Phys., 64,* 775.

Lundberg et al., E. T. (2011a), Multi-payload measurement of transverse velocity shears in the topside ionosphere, *Geophys. Res. Letts.*

Lundberg et al., E.T. (2011b), Multi-payload interferometric wavevector determination of auroral hiss, *J. Geophys. Res.*

Lynch, K. A., L. Gelinas, M. Kelley, and R. Collins, et al. (2005), Multiple sounding rocket observations of charged dust in the polar winter mesosphere, J. Geophys. Res., 110, doi:10.1029/2004JA010,502.

Lynch, K. A., J. L. Semeter, M. Zettergren, P. Kintner, R. Arnoldy, E. Klatt, J. LaBelle, R. Michell, E. MacDonald, and M. Samara (2007), Auroral ion outflow: low altitude energization, Annales Geophys., 25, 1967–1977.

Lynch, K. A., D. Hampton, M. Mella, B. Zhang, H. Dahlgren, M. Disbrow, P. M. Kintner, M. Lessard, E. Lundberg, and H. C. Stenbaek-Nielsen (2012), Structure and dynamics of the nightside poleward boundary: sounding rocket and groundbased observations of auroral electron precipitation in a rayed curtain, J. Geophys. Res., 117, doi:10.1029/2012JA017691.

Lynch, K. A., D. Hampton, M. Zettergren, and M. Lessard et al. (2013), Observations of gradient generated auroral ionopheric response effects, manuscript in preparation.

Lynch, K.A., (2013), ISINGLASS: Ionospheric Structuring: IN SItu and Groundbased Low Altitude StudieS, *Dartmouth College*, HTIDS-LCAS-ITM.

Lysak, R. L. (1985), Auroral electSrodynamics with current and voltage generators, J. Geophys. Res., 90, 4178.

Lysak, R. L. (1999), Propagation of Alfvén waves through the ionosphere: Dependence on ionospheric parameters, J. Geophys. Res., 104, doi:10.1029/1999JA900024.

Mella, M. R., K. A. Lynch, D. L. Hampton, H. Dahlgren, P. M. Kintner, M. Lessard, D. Lummerzheim, E. T. Lundberg, M. J. Nicolls, and H. C. Stenbaek-Nielsen (2011), Sounding rocket study of two sequential auroral poleward boundary intensications, J. Geophys. Res., 116, doi:10.1029/2011JA016,428.

Newell, P. T., T. Sotirelis, and S. Wing (2009), Diffuse, monoenergetic, and broadband aurora: The global precipitation budget, J. Geophys. Res., 114, doi:10.1029/2009JA014326.

Parks, G. K. (2004). Physics of space plasmas-an introduction, 2nd Edition. *Westview Press*.

Paschmann, G. (2002), Auroral Plasma Physics, Space Sci. Rev. – ISSI Monograph, 103.

Reiff, P. H. (1984), Models of auroral-zone conductances, in Magnetospheric Currents, AGU Monograph Series, vol. 28, edited by T. A. Potemra, p. 180, American Geophysical Union, Washington, DC.

Russell, A. J. B., A. N. Wright, and A. W. Hood (2010), Self-consistent ionospheric plasma density modifications by field-aligned currents: Steady state solutions, JGR, 115, doi: 10.1029/2009JA014836.

Russell, A. J. B., A. N. Wright, and A. V. Streltsov (2013), Production of small-scale Alfvén waves by ionospheric depletion, nonlinear magnetosphere-ionosphere coupling and phase mixing, JGR, 118, doi:10.1002/jgra.50168.

Siddiqui, M. U., L. E. Gayetsky, M. R. Mella, K. A. Lynch, and M. R. Lessard (2011), A laboratory experiment to examine the effect of auroral beams on spacecraft charging in the ionosphere, Physics of Plasmas, 18(9), 092905, doi:10.1063/1.3640512.

St-Maurice, J. P., & Schunk, R. W. (1977). Diffusion and heat flow equations for the mid-latitude topside ionosphere.

St.-Maurice, J., W. Kofman, and D. James (1996), In situ generation of intense parallel electric fields in the lower ionosphere, J. Geophys. Res., 101, 335–356, doi:10.1029/95JA02586.

Streltsov, A. V., and W. Lotko (2008), Coupling between density structures, electromagnetic waves and ionospheric feedback in the auroral zone, J. Geophys. Res., 113, doi:10.1029/ 2007JA012,594.

T Max Roberts, K Lynch, et al, A Small Spacecraft for Multipoint Measurement of Ionospheric Plasma, Rev. Sci. Inst., vol 88, 2017. Doi: 10.1063/1.4992022.

Torr, D. G., & Torr, M. R. (1979). Chemistry of the thermosphere and ionosphere. *Journal of Atmospheric and Terrestrial Physics*, *41*(7-8), 797-839.

Wolf, R. A. (1975). Ionosphere-magnetosphere coupling. *Space Science Reviews*, *17*(2-4), 537-562.

Zettergren, M., and J. Semeter (2012), Ionospheric plasma transport and loss in auroral downward current regions, Journal of Geophysical Research (Space Physics), 117(A16), A06306, doi: 10.1029/2012JA017637.

Zettergren, M., K. A. Lynch, and D. Hampton et al. (2013), Auroral ionospheric F-region cavity formation and persistence: effects of ion upflow, auroral driver inputs, and neutral winds, manuscript in preparation.